Delayed climate benefits and toxicity risks could hinder the sustainable deployment of enhanced weathering

Selene Cobo[1]* and Gonzalo Guillén-Gosálbez[2]

[1]Department of Chemical and Biomolecular Engineering, University of Cantabria, Spain

[2]Department of Chemistry and Applied Biosciences, Institute for Chemical and Bioengineering, ETH Zürich, Switzerland.

*cobos@unican.es

Abstract

Enhanced weathering has gained attention as a promising CO_2 removal (CDR) practice, but previous life cycle analyses rely on theoretical assumptions that differ substantially from experimental observations and overlook the risks of heavy metal emissions. Here, we draw on data from existing empirical studies to conduct a prospective life cycle assessment of multiple enhanced weathering scenarios. Our results indicate that experimental weathering rates lead to delayed climate benefits, with a median 11-year lag between rock application and the onset of net CDR for inland scenarios starting in 2030. This carbon payback period results from the initial peak in greenhouse gas emissions associated with the rock supply chain and processing activities. Furthermore, our probabilistic analysis indicates that basalt-derived zinc emissions could pose a greater toxicological risk than nickel release from dunite in the long term, potentially offsetting the health co-benefits of CDR and challenging the prevailing assumption that basalt is a safer feedstock. These findings suggest that the commercialization of CDR credits should be preceded by a thorough evaluation of near-term net climate benefits, and deployment should prioritize non-agricultural areas until field trials can more comprehensively assess the risks of food chain contamination.

Keywords: CO_2 removal, negative emissions, enhanced weathering, greenhouse gas removal efficiency, toxicity, human health, ecosystem quality

Introduction

Solely relying on emissions reductions will most likely be insufficient to limit global warming to 2 °C above pre-industrial levels. Scenarios assessed by the IPCC indicate that, in addition to deep and rapid decarbonization efforts, CO_2 removal (CDR) from the atmosphere will most likely be required to offset residual emissions and reverse a temporary temperature overshoot[1]. The timing of CDR deployment is therefore critical, and delays are expected to compound the technical and economic risks[2].

To scale up CDR at the required pace, a portfolio of Negative Emissions Technologies or Practices (NETPs) spanning a range of maturity levels is currently being developed[3]. Yet, previous studies have identified a range of sustainability trade-offs across CDR methods, most notably regarding health effects, planetary boundary transgressions, intensive resource demands, and the opportunity costs of energy allocation[4–6].

The health and environmental implications of enhanced weathering remain under-researched relative to other NETPs. This CDR approach accelerates natural weathering processes by grinding rocks containing silicate minerals and spreading them over land surfaces. The rock materials react with CO_2 in the presence of water (as illustrated by reaction R1 below, where *Me* represents a divalent metal) and drive the transfer of additional atmospheric CO_2 to the water[7]. Runoff transports the resulting alkalinity to the ocean, where the residence time of the sequestered dissolved inorganic carbon is on the order of 10^5 years[8–10].

The potential co-benefits of enhanced weathering–chiefly, the mitigation of soil and ocean acidification[8,11,12], improvement of soil structure and water retention[13], and increased soil fertility[14], which in turn augment biomass CDR[15]–render it attractive relative to other NETPs. Furthermore, enhanced weathering could present a thermodynamic advantage over other CDR methods; its energy demand–though highly scenario-specific and tied to variables such as grain size, transportation distances and rock type–has been estimated to be lower (<4 GJ/t CO_2[16]) than that of alternative NETPs such as direct air carbon capture and storage (<9 GJ/t CO_2[17,18]).

However, experimental studies mimicking field conditions remain limited and report weathering rates up to two orders of magnitude lower than previously estimated[13,19,20] due to multi-factorial constraints such as surface area, hydrology, biota and system feedbacks[21]. Moreover, the CDR potential of this NETP is highly dependent on site-specific conditions (such as temperature, moisture, and acidity[22,23]), and part of the removed CO_2 could be released back to the atmosphere via the secondary precipitation of mineral carbonates if the system reaches

supersaturation (R2), or through the reaction of acidic species with the generated bicarbonate ions (R3)[24–26]. In addition to these geochemical uncertainties, it has been suggested that rock weathering may not yield inorganic CDR within short timescales[27]. Lastly, toxic heavy metals can also be released as the rock particles dissolve[28–30]. While experimental studies with basalt have not raised concerns about dangerously high heavy metal concentrations[31–35], nickel levels above regulatory limits have been found when olivine is used[36,37].

$$Me_2SiO_4 + 4CO_2 + 4H_2O \rightarrow 2Me^{2+} + 4HCO_3^- + H_4SiO_4 \quad \text{(R1)}$$

$$Me^{2+} + 2HCO_3^- \rightarrow MeCO_3 + CO_2 + H_2O \quad \text{(R2)}$$

$$H^+ + HCO_3^- \rightarrow CO_2 + H_2O \quad \text{(R3)}$$

Previous Life Cycle Assessment (LCA) studies quantifying the environmental impacts of enhanced weathering overlook these issues. They rely on estimated CO_2 sequestration potentials[38–43] or theoretical weathering rates[44–47] instead of experimental data. Furthermore, most of them disregard the risk of heavy metal leaching, with only one work[41] assessing the impacts of nickel release following the application of olivine-rich rocks on coastal areas.

Despite all the uncertainties surrounding the performance of this NETP[48,49], there has been a surge in enhanced weathering start-ups selling CDR credits[50,51]. Thus, ascertaining the implications of enhanced weathering for human health and the environment is critical to ensure that it can be responsibly deployed[52].

Here, we investigate the greenhouse gas removal (GGR) efficiency of enhanced weathering and its potential impacts on human health and ecosystems. Our analysis–grounded in reported experimental results and a comprehensive accounting of unintended emissions–assesses how applying rock particles with different compositions across various environments would affect these outcomes.

Scenarios

We model 14 scenarios involving the application of rock particles on coastal and inland (croplands and forestlands) areas, using weathering rates derived from theoretical[53], laboratory[54–56], mesocosm[32,36] and field[31] studies, which were normalized to a reference temperature of 15 °C. Given the varying experimental and environmental conditions across studies (summarized in Table S3 of the Supporting Information), we aim to establish a

representative range of performance indicators for enhanced weathering, rather than conducting a direct comparative analysis of individual studies.

Our life cycle inventories comprise mining operations, rock transportation, comminution, and spreading, as well as the emissions occurring as the rocks weather over the considered 100-year time horizon. We focus on two rock types: basalt and dunite. Although each presents a distinct set of metal concentrations (see Tables 1.1 and 1.2 of the Supporting Data[57]), previous studies assume that basalt poses fewer risks than dunite because of its lower nickel and chromium content[14,58,59].

In cropland scenarios, we consider the phosphorus released from rock particles to substitute for an equivalent amount of synthetic phosphate fertilizers, thereby reducing fertilizer inputs while keeping crop yields constant relative to the baseline without rock application. By contrast, we assume that forest scenarios receive no industrial fertilizers; therefore, increased phosphorus availability enhances biomass carbon uptake relative to the baseline. Notably, we do not consider fertilization effects in the coastal scenarios given the many uncertainties regarding the efficiency and permanence of the carbon sequestration[60–62]. Further details on the scenarios' characteristics and enhanced weathering models are in Section 3 of the Supporting Information.

Our models are aligned with climate change mitigation projections generated by the REMIND[63] 3.5 integrated assessment model. We focus on scenario SSP2-PkBudg1000, which assumes a middle-of-the-road shared socio-economic pathway (SSP2)[64] and a peak carbon budget of 1,000 Gt CO_2eq, limiting global warming to 1.7-2.0 °C by 2100. We also test the sensitivity of our results to alternative climate trajectories based on Nationally Determined Contributions (SSP2-NDC) and National Policy implementations (SSP1-NPi), which lead to a temperature increase of 2.0-2.5 °C above pre-industrial levels.

Methods

We conduct an attributional[65] prospective[66] LCA using *Brightway* 2.5[67] and the *premise*[68] 2.3.3 python library to adapt activities in the Ecoinvent[69] 3.11 database to scenario projections from REMIND[63] 3.5.

The functional unit is defined as the gross geochemical removal of 100 Mt CO_2 in one year through enhanced weathering reactions–excluding additional CDR from biomass fertilization

effects to ensure a consistent cross-scenario comparison. Embedding the temporal dimension in the definition of the functional unit is essential to reflect how weathering kinetics–and not merely intrinsic alkalinity–determine the mass of rock required to achieve a given CDR target within a specific timeframe. The proposed functional unit represents 26% of the total CDR projected for 2030 in the selected reference mitigation scenario and falls within techno-economic constraints[70,71], as detailed in Section 3.3 of the Supporting Information.

We calculate the time-dependent GGR efficiency of enhanced weathering ($GGR\eta_{t,y}$) as the ratio between the net amount of CO_2eq removed (i.e., the difference between the atmospheric CO_2 sequestered after reacting with silicate minerals and the CO_2eq emitted throughout the rocks' life cycle) and the total amount of CO_2 removed from the atmosphere via enhanced weathering reactions *t* years after the rock particles are applied to the soil in year *y*–as shown in Equation E1, where $CDR_{s,t,y}$ and $GHG_{s,t,y}$ represent the gross amount of substance *s* within the set $J$of greenhouse gases that is either removed or emitted in year *t* after the year *y* of deployment (assumed to be 2030 or 2050). The dynamic global warming potential ($GWP_{s,t}$, estimated with Equations SE1-5 in the Supporting Information and based on [72]) reflects that CDR near the end of the 100-year time horizon prevents less warming than CDR at the beginning.

$$GGR\eta_{t,y} = \frac{\sum_{t'=0}^{t'=t} \sum_{s\in J} (\left|CDR_{s=CO_2,t',y}\right| - GHG_{s,t',y}) \cdot GWP_{s,t'}}{\sum_{t'=0}^{t'=t} \left|CDR_{s=CO_2,t',y}\right|} \quad \forall\, t \in T, y \in Y \qquad \text{(E1)}$$

We quantify damage to human health and ecosystems relative to a baseline without CDR using the hierarchist perspective of the ReCiPe 2016 method[73]. Health impacts, aggregated over the time horizon, are expressed in Disability-Adjusted Life Years (DALYs), representing the years of healthy life lost due to disability or premature death. Ecosystem impacts are quantified as the local species loss aggregated over space and time, expressed in species·year.

We assume a 50% release rate for phosphorus and metals from annually weathered rocks in our base scenarios, while exploring the full range (0 to 100%) within our uncertainty analysis. We estimate the health and ecosystem impacts averted by phosphorus fertilization differently for each scenario location. In cropland scenarios, these co-benefits are linked to the avoided production of synthetic phosphate fertilizers, consistent with the avoided burden LCA method[65]. In forest scenarios, prevented health and ecosystem impacts arise from the secondary CO_2 sequestered by the phosphorus-induced biomass growth (1.6-6.7 kg C/kg P[74]).

CDR prevents health and ecosystem impacts linked to the averted rise in global temperatures[5,6]. These co-benefits (alongside those related to the substitution of industrial fertilizers in the cropland scenarios) may be–partially or entirely–offset by the health and ecosystem impacts associated with the resources used and pollutants emitted throughout the enhanced weathering systems and their underlying supply chains. Hence, we define net health and ecosystem damage as the balance between the impacts generated and avoided by CDR (equations SE6 and SE7 in the Supporting Information); positive values imply that undesired impacts outweigh co-benefits, and negative values indicate that prevented impacts are greater than detrimental side-effects.

We use Equation E2 to calculate $MT^{H}_{n,ec}$, i.e., the human toxicity effects of metal emissions to environmental compartment *ec* (seawater, agricultural soil, or forest soil, depending on the scenario location) due to the annual weathering of rock *n* (DALY/year). Here, RM^{A}_{n} represents the mass of rock *n* that weathers annually (kg/year), $C_{s,n}$ is the concentration of substance *s* within the set ME of metals in rock *n* (kg/kg), $f_{s,ec}$ denotes the fraction of metal *s* emitted to environmental compartment *ec*, and $TF^{C}_{s,ec}$ and $TF^{NC}_{s,ec}$ are the carcinogenic and non-carcinogenic toxicity factors for metal *s*, respectively, provided by the ReCiPe 2016 method[73] (DALY/kg). Toxicity factors account for the environmental persistence and bioavailability of the emitted metals. Notably, long-term metal intake is primarily driven by dietary ingestion[75], as detailed in Section 2.2 of the Supporting Information.

$$MT^{H}_{n,ec} = \sum_{s \in ME} RM^{A}_{n} \cdot C_{s,n} \cdot f_{s,ec} \cdot (TF^{C}_{s,ec} + TF^{NC}_{s,ec}) \quad \forall\, n \in N, ec \in EC \tag{E2}$$

To estimate the probability distributions of the human toxicity impacts associated with metal emissions, we perform 10,000 Monte Carlo simulations in which RM^{A}_{n}, $C_{s,n}$ and $f_{s,ec}$ are sampled from uniform distributions, which avoids introducing unsupported assumptions by treating all values within the plausible range as equally likely. $f_{s,ec}$ changes between 0 and 1 to account for metal mobilization driven by possible fluctuations in soil pH and redox potential[76], RM^{A}_{n} varies between the minimum and maximum values estimated across the inland scenarios modeled for each rock type, and $C_{s,n}$ takes values within the ranges reported in the literature[36,77–79].

Figure 1 outlines the methodological sequence followed in this study. Additional data and assumptions underpinning our models are described in Section 3 of the Supporting Information. Life cycle inventories are compiled in the Supporting Data[57].

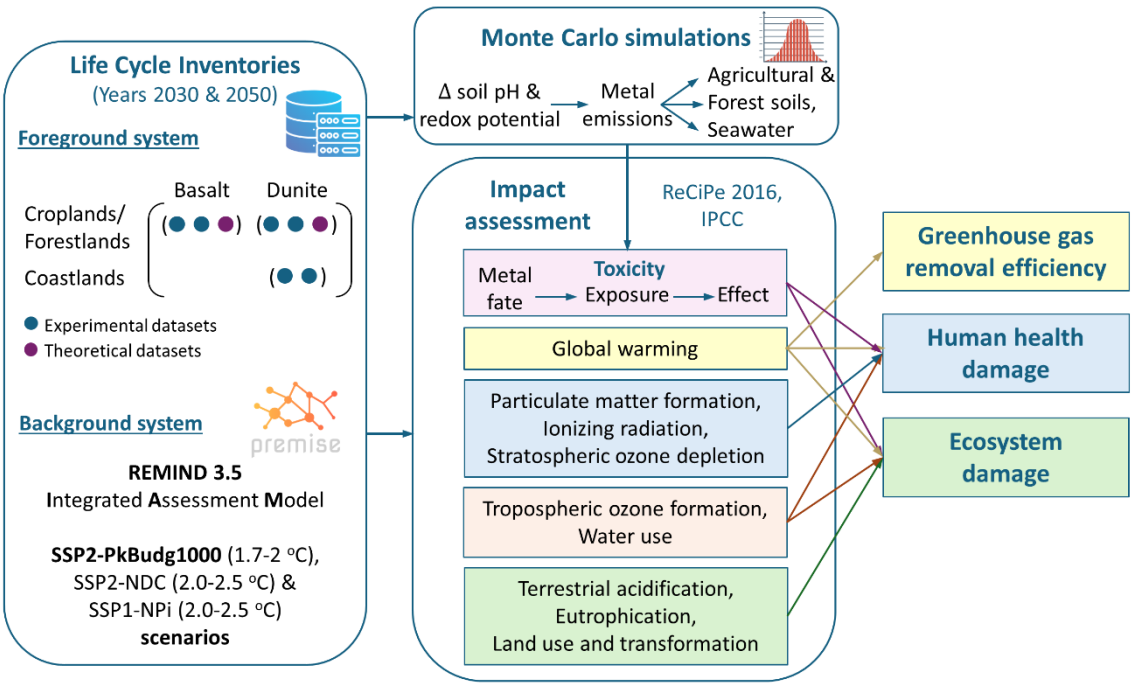

Fig. 1. Data flow and integrated methodological framework used for the prospective life cycle assessment of the enhanced weathering scenarios.

Results

Delay in climate benefits

Figure 2 illustrates how the GGR efficiencies of our scenarios improve as the rocks progressively weather over time, increasing CDR. GGR efficiencies are dictated by the weathering rates, with scenarios considering theoretical kinetic data achieving better outcomes than those based on the slower rates reported in experimental studies. As expected, in the theoretical scenarios assuming identical particle sizes and soil conditions, dunite outperforms basalt because of its higher alkalinity content, which implies that less rock is required to achieve the same CDR (Supporting Figure S2). We also observe lower GGR efficiencies for scenarios starting in 2030 (Figure 2a) relative to 2050 (Figure 2b), as the gradual adoption of decarbonization measures increasingly reduces the carbon footprint of the activities involved in the rock supply chains.

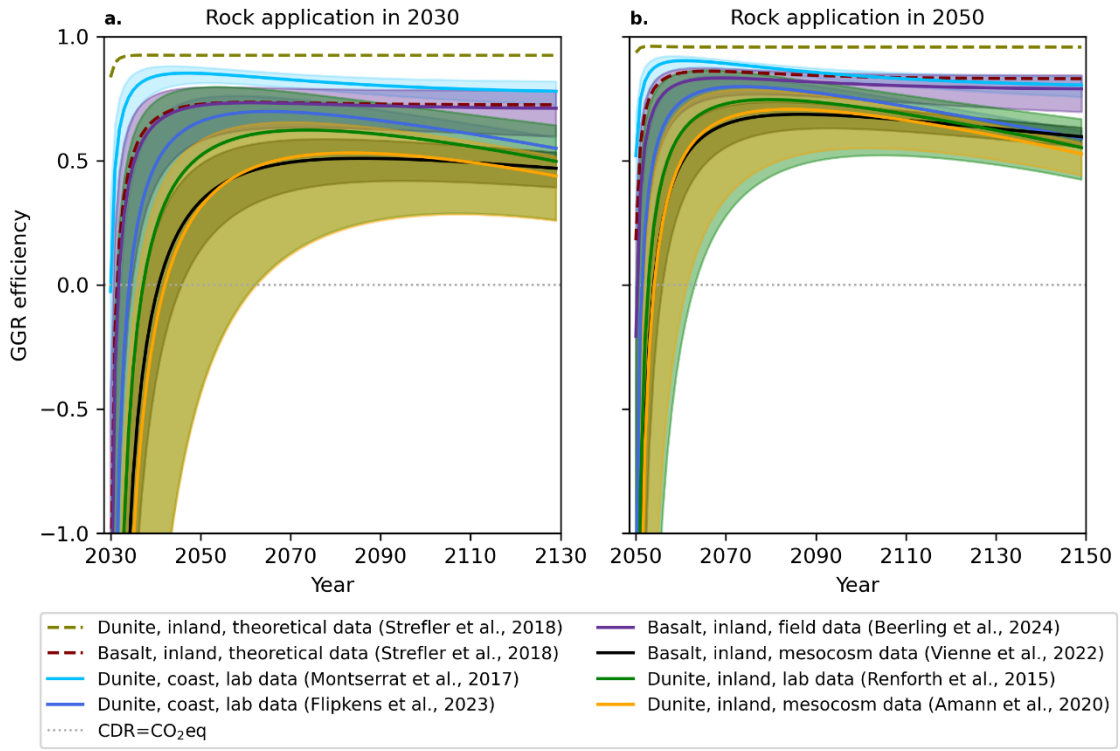

Fig. 2. Evolution of greenhouse gas removal (GGR) efficiencies over 100 years, considering experimental[31,32,36,54–56] and theoretical[53] data for the application of dunite and basalt on coastal and inland environments. The shaded areas represent the uncertainty in the results. **a** Single rock application in 2030. **b** Single rock application in 2050.

In the inland scenarios modeled after experimental results, initial CDR is insufficient to offset greenhouse gas emissions associated with rock extraction, transportation, and processing, which are assumed to occur in the year that the rock particles are applied to the soil. Indeed, these experimental scenarios only attain positive GGR efficiencies (removing more CO_2eq than

is emitted) 2-14 years after the rock application (central values), with the exact timing depending on the scenario and year of deployment. If the least favorable parameters are considered, it takes up to 34 years for rock particles applied in 2030 to achieve net CDR.

While the inland scenarios based on experimental data from [32,36,56] achieve modest GGR efficiencies by the end of the 100-year time horizon (0.44-0.60, central values), the scenario considering data from a field trial with basalt[31] yields higher GGR efficiencies (0.71-0.79), similar to those of the scenario relying on theoretical basalt weathering rates. Indeed, this is the only scenario based on experimental data that achieves complete weathering within 100 years (Supporting Figure S3 and Table S4). This discrepancy could be attributed to differences in the methods used to quantify weathering rates; studies [32,36,56] determined these rates based on alkalinity concentrations in the effluent of the experimental set-ups, whereas [31] relies on the residual cation content measured in soils. This soil-based technique assumes that all cation losses lead to CDR, overlooking cation uptake by plants and formation of secondary minerals[51].

The coastal enhanced weathering scenario based on [54] does not show a significant delay in the climate benefits, achieving GGR efficiencies of 0.73-0.84 at the end of the 100-year time horizon. By contrast, the coastal scenario modeled after [55] attains worse results (positive GGR efficiencies 2-9 years after the rock application, reaching values of 0.50-0.62 after 100 years), although it outperforms the inland scenarios using the same rock type. This could be in part due to the advantageous conditions of the simulated coastal environments, where dunite particles were directly subjected to agitation in seawater, omitting the initial transport phase.

The theoretical scenarios attain the highest GGR efficiencies for each rock type (0.73-0.96 at the end of the studied period). Notably, GGR efficiencies in the dunite theoretical scenarios stabilize shortly after the initial peak in emissions because weathering happens quickly. Here, 100% of dunite grains have weathered 14 years after being applied, while basalt reaches this point 70 years after the rock application (Supporting Figure S3 and Table S4). Conversely, the GGR efficiency curves for the scenarios based on experimental data present a slight decline after reaching their maximum values. The reason is that the denominator of the GGR efficiency (Equation E1) grows faster than the numerator because the dynamic global warming potential progressively decreases over time, becoming 0 at the end of the time horizon.

Results for enhanced weathering scenarios aligned with alternative climate change mitigation pathways (Supporting Figure S4) follow the same patterns but exhibit variability in GGR efficiencies relative to SSP2-PkBudg1000 (Figure 1). Specifically, efficiencies decrease by up to

20% at the end of the studied period under the SSP1-NPi scenario, whereas they increase by up to 18% under the SSP2-NDC pathway. The latter enforces more aggressive decarbonization targets, thereby reducing the upstream greenhouse gas emissions associated with rock processing and transport.

Health and ecosystem co-benefits offset by life cycle emissions

Here we evaluate how human health and ecosystem quality are affected by the gross removal of 100 Mt CO_2 in 2030 (Figure 3a) and 2050 (Figure 3b). We assume a regime of consecutive annual deployments, where rock particles are initially applied in 2030, and the amount of rock weathered the previous year must be subsequently applied to maintain a constant CDR rate (details in Section 3.1 of the Supporting Information). Hence, the bulk of the rock processing activities occur in 2030, which is reflected in the worse environmental performance of the analyzed scenarios in the initial year.

In 2030, health and ecosystem impacts correlate inversely with GGR efficiencies, with the most efficient scenarios yielding the lowest overall damage. Inland scenarios based on mesocosm and laboratory experiments[32,36,56] cause the most harmful effects during the initial year of deployment ($2.4{\cdot}10^6$-$3.6{\cdot}10^6$ DALYs and $5.4{\cdot}10^3$-$7.9{\cdot}10^3$ species·year), which are comparable in magnitude to 0.8-1.2% of the damage caused by COVID-19 in 2021[80] and to the loss of 0.3-0.5% of the world's terrestrial species in one year[73]. Notably, only the theoretical dunite scenarios avert net health and ecosystem damage during the first year of rock application. In these cases, the CDR co-benefits are enough to counterbalance the undesired consequences of resource use and pollutant emissions on human health and ecosystems.

Conversely, in 2050 all scenarios prevent net ecosystem impacts (between $2.0{\cdot}10^2$ and $2.6{\cdot}10^2$ species·year), with the basalt scenarios exhibiting the worst outcomes. Only the three scenarios considering basalt spreading on croplands generate net health damage (≤$1.6{\cdot}10^5$ DALYs). Notably, basalt exhibits a wider variance than dunite across application environments.

The poorer performance of basalt scenarios in 2050 can partially be explained by basalt's lower alkalinity content, which entails that larger amounts of rock must be weathered to achieve the same annual CDR as dunite, leading to higher upstream impacts. This scenario ranking deviates from that of 2030, where the best-performing inland scenarios based on experimental results corresponds to the basalt dataset with the highest temperature-normalized alkalinity dissolution

rate (derived from [31]), whereas the dunite scenario with the lowest dissolution rate (data from [36]) is the most damaging.

Equations SE12-14 in the Supporting Information explain these divergent trends. While the amount of rock that must be applied in the initial year of deployment is inversely proportional to the alkalinity dissolution rates, in subsequent years the amount of rock that has been weathered–and must therefore be reapplied to maintain a constant annual CDR–is inversely proportional to the rock's alkalinity concentration. We note that health and ecosystem impacts projected for alternative mitigation pathways (Supporting Figure S5) follow the same trends, varying between -14% and +7% compared to the climate mitigation scenario considered here.

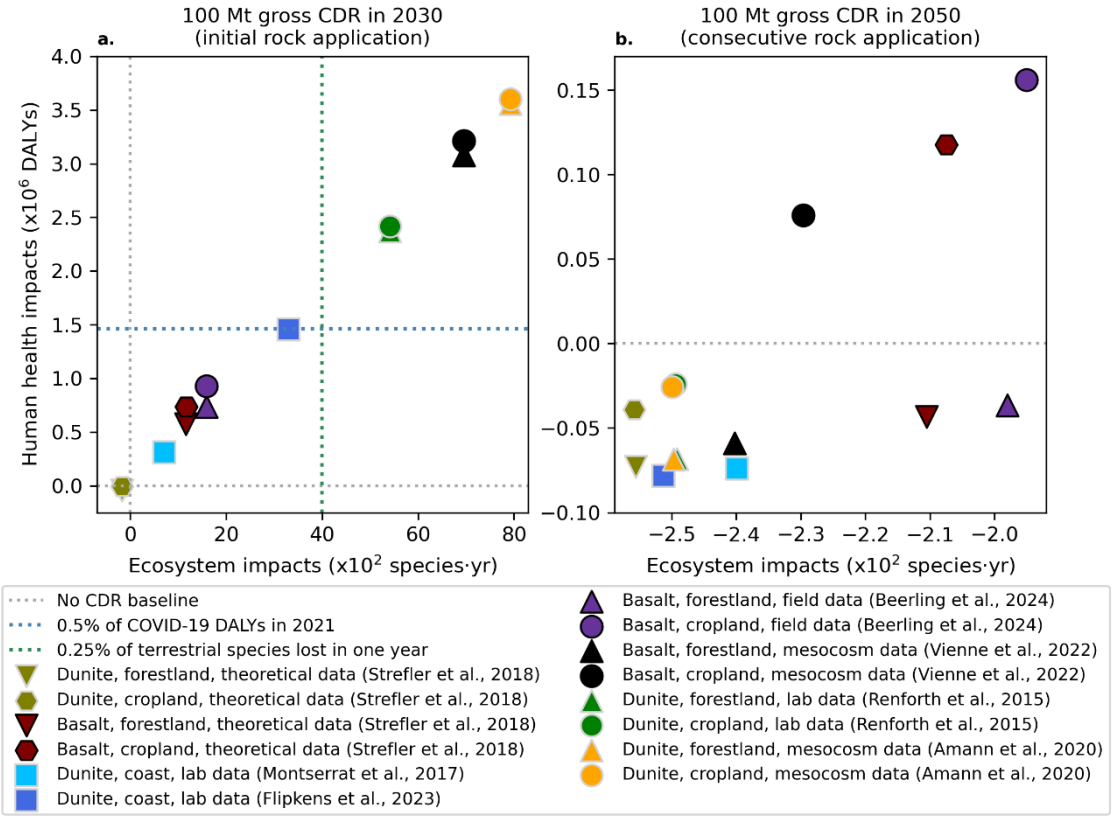

Fig. 3. Human health and ecosystem impacts of removing 100 Mt CO_2 (gross) in 2030 and 2050, considering experimental[31,32,36,54–56] and theoretical[53] data for the application of dunite and basalt on coastal and inland (forestlands and croplands) environments. **a** Rock application in 2030 for the first time. **b** Consecutive rock application in 2050.

Figure 4 displays the disaggregated health impacts of two representative inland scenarios based on data from mesocosm experiments for basalt[32] and dunite[36], with results tied to the unique experimental conditions of each study. In the initial year of rock application (2030), >99% of the undesired health impacts in both scenarios arise from the greenhouse gases, particulate matter and toxic substances emitted throughout the rock supply chains and processing activities–over

64% of which are linked to rock transportation (road transport distances of 180-250 km[81]). In the selected scenarios, the health impacts of removing 100 gross Mt CO_2 with basalt (Figure 4a) and dunite (Figure 4d) in 2030 amount to $3.1 \cdot 10^6$ ($2.2 \cdot 10^6$, $4.4 \cdot 10^6$) and $3.6 \cdot 10^6$ ($1.9 \cdot 10^6$, $8.4 \cdot 10^6$) DALYs, respectively.

After the initial year of rock application–when most of the rocks are mobilized–health outcomes are primarily determined by the potential metal release and the CDR co-benefits. Our results challenge the common assumption that basalt is safer than dunite, showing that the metals contained in basalt could lead to greater health problems. Zinc emissions from basalt grains applied to croplands can cause significant non-carcinogenic toxicity effects, leading to net health damage in 2050: $7.6 \cdot 10^4$ ($-8.4 \cdot 10^4$, $3.3 \cdot 10^5$) DALYs due to the removal of 100 gross Mt CO_2 (Figure 4b). Dunite can also emit zinc in lower amounts, but nickel–conducive to carcinogenic toxicity impacts–poses a greater health risk with this rock. Nevertheless, the health co-benefits of CDR could offset the toxicity effects of metal release from dunite, preventing net damage; the health impacts of removing 100 Mt CO_2 by applying dunite to croplands in 2050 amount to $-2.6 \cdot 10^4$ ($-8.0 \cdot 10^4$, $4.4 \cdot 10^4$) DALYs (Figure 4e).

Spreading rock grains in forests is less hazardous to humans because of the lower risk of metals entering the food supply chain. The gross removal of 100 Mt CO_2 in 2050 with basalt applied to forestland can also avert net health damage, i.e., $-5.9 \cdot 10^4$ ($-8.9 \cdot 10^4$, $-2.8 \cdot 10^4$) DALYs (Figure 4c), similar to the net impacts prevented with dunite: $-6.9 \cdot 10^4$ ($-8.0 \cdot 10^4$, $-5.4 \cdot 10^4$) DALYs (Figure 4f). By contrast, if nickel is released into coastal environments at high rates such as those reported in [54], the associated toxicity effects could offset as much as 91% of the health co-benefits of CDR in the initial year of deployment (Supporting Figure S6).

As Supporting Figure S7 shows, the damage to ecosystem quality due to metal release is negligible in the experimental inland scenarios, where >66% of detrimental ecosystem impacts are attributed to global warming and land use associated with rock transportation and quarry operations. The difference in ecosystem damage between croplands and forestlands is driven primarily by the distinct fertilization effects of phosphorus release in these environments. Conversely, the ecotoxicity effects of nickel emissions could play a more important role in marine environments, offsetting up to 87% of the CDR ecosystem co-benefits of the coastal enhanced weathering scenarios in 2030 (Supporting Figure S6).

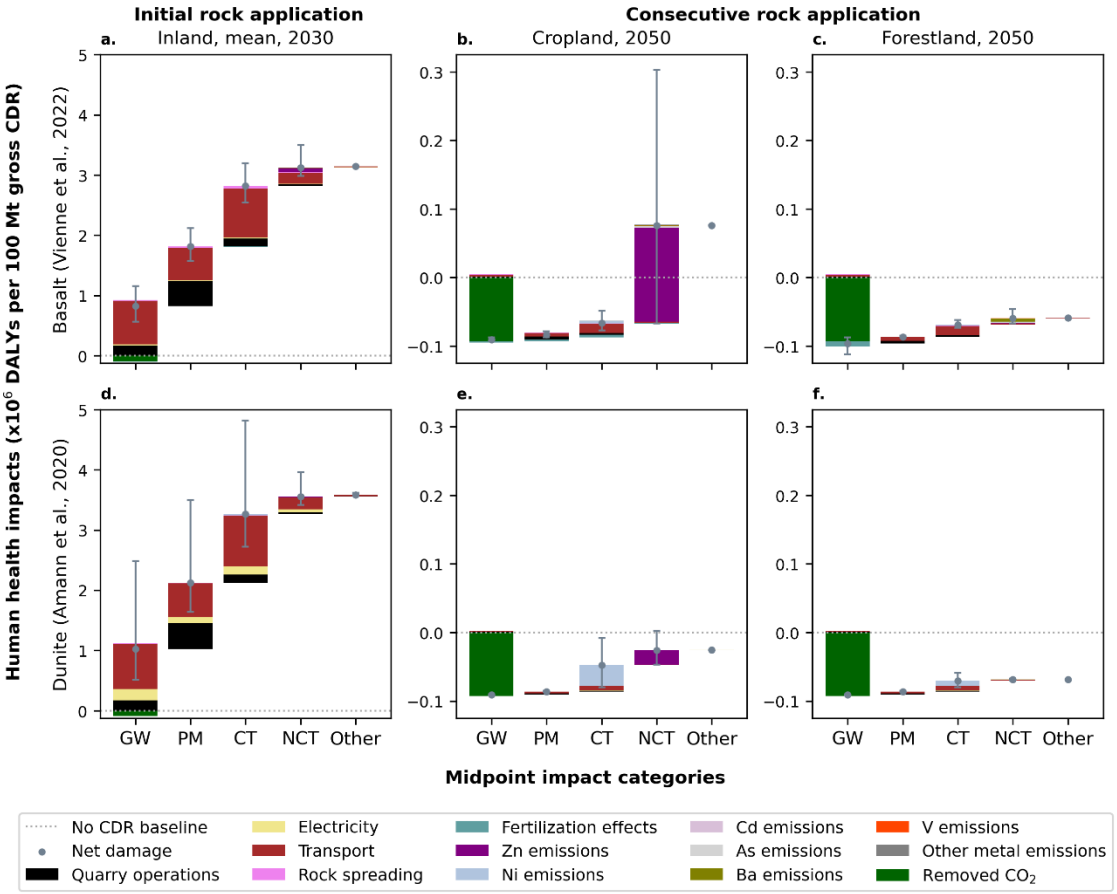

Fig. 4. Human health impacts of removing 100 Mt CO_2 (gross) in 2030 and 2050, considering initial rock application in 2030 and consecutive applications in subsequent years. Data from [32,36]. Error bars represent the uncertainty in the results. Impacts disaggregated by the contribution of i) unit processes and direct emissions, and ii) environmental mechanisms: global warming (GW), fine particulate matter formation (PM), carcinogenic toxicity (CT), non-carcinogenic toxicity (NCT), and others (tropospheric ozone formation, stratospheric ozone depletion, ionizing radiation, and water consumption). **a** Basalt application to cropland/forestland (mean), 2030. **b** Basalt application to cropland, 2050. **c** Basalt application to forestland, 2050. **d** Dunite application to cropland/forestland (mean), 2030. **e** Dunite application to cropland, 2050. **f** Dunite application to forestland, 2050.

Basalt entails higher toxicity risks than dunite in the long term

Potential metal release to agricultural soils introduces significant uncertainty into the human toxicity assessment (Figure 4). To address this knowledge gap in the long-term fate of metals, we conduct Monte Carlo simulations characterizing the probability distribution of toxicity impacts associated with metal emissions from basalt and dunite applied to croplands (Figure 5).

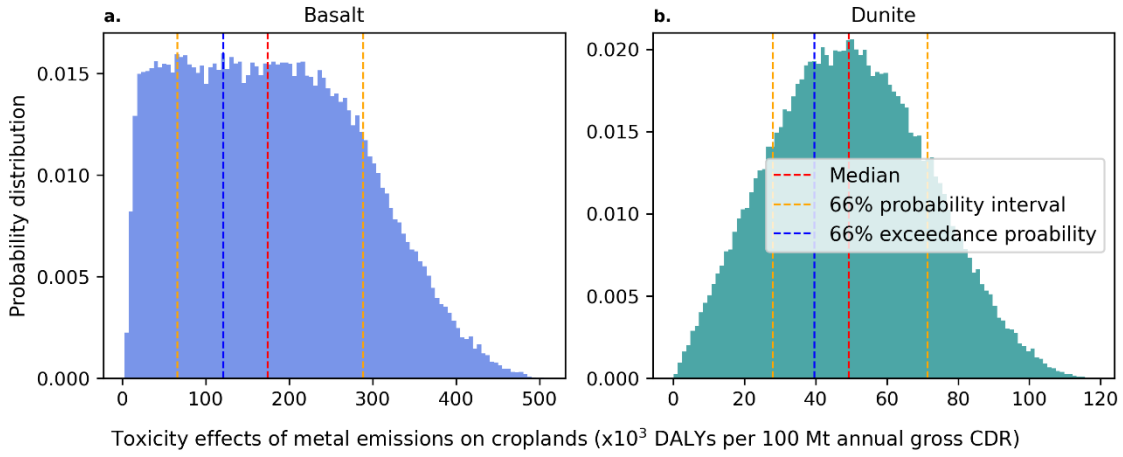

Fig. 5. Probability distributions of toxicity-driven human health impacts from metal emissions to agricultural soil, calculated with the hierarchist perspective of the ReCiPe 2016 method. Data represent Monte Carlo simulation results for the annual removal of 100 Mt CO_2 (gross) using **a** Basalt. **b** Dunite.

We find that deploying basalt and dunite to remove 100 Mt CO_2 entails a 66% likelihood that associated metal emissions would lead to health impacts exceeding $1.2{\cdot}10^5$ and $4.0{\cdot}10^4$ DALYs, respectively. The median health toxicity effects linked to metal release from basalt are $1.7{\cdot}10^5$ DALYs (66% likelihood: $6.6{\cdot}10^4$-$2.9{\cdot}10^5$ DALYs, Figure 5a), 3.5 times the impacts associated with dunite, i.e., $4.9{\cdot}10^4$ DALYs (66% likelihood: $2.8{\cdot}10^4$-$7.1{\cdot}10^4$ DALYs, Figure 5b). Although the toxicity effects of basalt are more dispersed than those of dunite (coefficients of variation: 0.58 and 0.43, respectively), the low overlap between the likely toxicity ranges of the two rocks highlights the higher risks of basalt.

The probability distribution of basalt's toxicity effects is virtually flat shaped across a wide range of values, consistent with the underlying uniform distributions. Since uniformly distributed variables are combined multiplicatively (equation E2), combinations of high values reinforce one another, producing large outcomes. This amplification stretches the right tail of the distribution and generates the observed positive skewness.

By contrast, the dunite distribution follows a highly symmetric and unimodal shape, indicating that outcomes near the median are significantly more likely than extreme values. Although the metal emissions from dunite follow uniform distributions (Supporting Figure S8), its aggregate

toxicity effects are dominated by two metals–nickel and zinc–with different characterization factors, whereas basalt's toxicity is mainly driven by zinc (Figure 4). Hence, the combination of distinct toxicity contributors in dunite leads to a probability distribution converging toward a Gaussian shape, consistent with the central limit theorem[82].

The metal-induced toxicity effects depicted in Figure 5 are calculated using characterization factors that reflect impact mechanisms based on current scientific consensus and a 100-year time horizon. Nevertheless, metal toxicity impacts are highly dependent on the selected timeframe[40]. As shown in Supporting Figure S9, alternative value choices–regarding time horizons and acceptable degrees of scientific evidence–yield different results.

Notably, if a precautionary framework based on an infinite time horizon is adopted, the toxicity impacts of both rocks increase by one order of magnitude. By contrast, under a 20-year techno-optimistic perspective, the human toxicity impacts of dunite and basalt are one and three orders of magnitude lower than in the consensus-based perspective, respectively.

Under the optimistic perspective, basalt is preferable to dunite. The reason is that nickel poses a greater risk than zinc via inhalation and drinking water consumption–the only human exposure routes considered in the short term. Conversely, over longer timelines where exposure via food intake is accounted for, the bioaccumulation of zinc in food products causes basalt's integrated toxicity score to overtake that of dunite.

Discussion

Our analysis reveals the potential risks of relying on enhanced weathering for immediate climate benefits. Notably, inland scenarios based on experimental weathering rates show a median 11-year lag between the initial rock application in 2030 and the onset of net CDR. Although the estimated delay remains sensitive to the uncertainties inherent in the weathering rate measurement techniques used in the considered experimental studies, our results suggest that representative weathering rates may be insufficient to offset the peak in greenhouse gas emissions associated with the rock supply chain and processing activities within climate-relevant timeframes. Such delays in net CDR imply that enhanced weathering should not be viewed as an emergency intervention to rapidly shorten the duration of a temporary temperature overshoot, as the initial carbon debt could lead to additional warming in the near term.

While these kinetic barriers could be bridged–via optimal grain size[83], site selection[84], irrigation[85], pH management[84,86], or the integration of biological accelerators such as mycorrhizal fungi[87]–the potential health risks associated with metal leaching remain a concern. Our probabilistic analysis reveals that the long-term toxicity effects of basalt applied to croplands–primarily driven by zinc emissions–are greater than those of the dunite needed to achieve the same CDR and could counteract the health co-benefits of negative emissions. Thus, these findings challenge the notion that basalt is safer because of its lower nickel content.

Even if new research suggests that harmful metals are largely retained in the soil over meaningful timescales, their eventual release remains sensitive to future perturbations in the soil pH and redox conditions[76]. These changes are driven by an interplay of physicochemical and biological processes[76,88] that are difficult to monitor and regulate at scale–such as atmospheric deposition and the resulting soil acidification, or soil respiration, which alters CO_2 and oxygen levels in pore water. Consequently, it is essential to include potential metal emissions in life cycle and risk assessments. Future studies should investigate potential mixed-metal 'cocktail effects' to determine whether concurrent metal releases compound cumulative toxicity[89].

Despite these uncertainties, the likelihood of trace-metal mobilization triggered by redox shifts could be reduced by avoiding areas with low pH buffering capacity[90] and poorly drained soils[91]. However, given the complexity of soil biogeochemistry and based on these preliminary results, it may be advisable to adopt a precautionary approach by prioritizing non-agricultural areas for enhanced weathering trials. This could mitigate the projected risk of toxic heavy metals entering the food supply chain, thereby minimizing the potential for human exposure.

Our findings highlight that a robust monitoring, reporting, and verification framework, underpinned by field-scale evidence, remains essential to safeguard the integrity of carbon markets. Until kinetic lags and heavy metal dynamics are better understood, the sale of CDR credits from enhanced weathering may be premature. In the interim, investments should target pilot deployments designed to resolve these uncertainties and lay the scientific foundation for a safe and sustainable CDR industry.

Associated content

The data supporting these findings are available in the Supporting Information and the Supporting Data[57] (https://doi.org/10.5281/zenodo.16094445).

Acknowledgements

S.C. acknowledges financial support from grant RYC2022-035377, funded by MICIU/AEI/10.13039/501100011033 and the ESF+.

References

(1) IPCC. Climate Change 2022: Mitigation of Climate Change. Contribution of Working Group III to the Sixth Assessment Report of the Intergovernmental Panel on Climate Change; 2022. https://doi.org/10.1017/9781009157926.

(2) Galán-Martín, Á.; Vázquez, D.; Cobo, S.; Mac Dowell, N.; Caballero, J. A.; Guillén-Gosálbez, G. Delaying Carbon Dioxide Removal in the European Union Puts Climate Targets at Risk. Nature Communications **2021**, 12 (1), 6490. https://doi.org/10.1038/s41467-021-26680-3.

(3) Cobo, S.; Negri, V.; Valente, A.; Reiner, D. M.; Hamelin, L.; Dowell, N. M.; Guillén-Gosálbez, G. Sustainable Scale-up of Negative Emissions Technologies and Practices: Where to Focus. Environ. Res. Lett. **2023**, 18 (2), 023001. https://doi.org/10.1088/1748-9326/acacb3.

(4) Jacobson, M. Z.; Fu, D.; Sambor, D. J.; Mühlbauer, A. Energy, Health, and Climate Costs of Carbon-Capture and Direct-Air-Capture versus 100%-Wind-Water-Solar Climate Policies in 149 Countries. Environ. Sci. Technol. **2025**, 59 (6), 3034–3045. https://doi.org/10.1021/acs.est.4c10686.

(5) Cobo, S.; Galán-Martín, Á.; Tulus, V.; Huijbregts, M. A. J.; Guillén-Gosálbez, G. Human and Planetary Health Implications of Negative Emissions Technologies. Nature Communications **2022**, 13 (1), 2535. https://doi.org/10.1038/s41467-022-30136-7.

(6) Cobo, S.; Galán-Martín, Á.; Guillén-Gosálbez, G. Negative Emissions Technologies and Practices Could Challenge Global Resource Supply and Environmental Limits. Commun Earth Environ **2026**, 7 (354). https://doi.org/10.1038/s43247-026-03348-8.

(7) Hartmann, J.; West, A. J.; Renforth, P.; Köhler, P.; De La Rocha, C. L.; Wolf-Gladrow, D. A.; Dürr, H. H.; Scheffran, J. Enhanced Chemical Weathering as a Geoengineering Strategy to Reduce Atmospheric Carbon Dioxide, Supply Nutrients, and Mitigate Ocean Acidification. Reviews of Geophysics **2013**, 51 (2), 113–149. https://doi.org/10.1002/rog.20004.

(8) Renforth, P.; Henderson, G. Assessing Ocean Alkalinity for Carbon Sequestration. Reviews of Geophysics **2017**, 55 (3), 636–674. https://doi.org/10.1002/2016RG000533.

(9) Middelburg, J. J.; Soetaert, K.; Hagens, M. Ocean Alkalinity, Buffering and Biogeochemical Processes. Reviews of Geophysics **2020**, 58 (3), e2019RG000681. https://doi.org/10.1029/2019RG000681.

(10) Archer, D. Fate of Fossil Fuel CO_2 in Geologic Time. J. Geophys. Res. **2005**, 110 (C9), 2004JC002625. https://doi.org/10.1029/2004JC002625.

(11) Taylor, L. L.; Quirk, J.; Thorley, R. M. S.; Kharecha, P. A.; Hansen, J.; Ridgwell, A.; Lomas, M. R.; Banwart, S. A.; Beerling, D. J. Enhanced Weathering Strategies for Stabilizing Climate and Averting Ocean Acidification. Nature Climate Change **2016**, 6 (4), 402–406. https://doi.org/10.1038/nclimate2882.

(12) Vakilifard, N.; Kantzas, E. P.; Edwards, N. R.; Holden, P. B.; Beerling, D. J. The Role of Enhanced Rock Weathering Deployment with Agriculture in Limiting Future Warming and Protecting Coral Reefs. Environmental Research Letters **2021**, 16 (9), 094005. https://doi.org/10.1088/1748-9326/ac1818.
(13) Calabrese, S.; Wild, B.; Bertagni, M. B.; Bourg, I. C.; White, C.; Aburto, F.; Cipolla, G.; Noto, L. V.; Porporato, A. Nano- to Global-Scale Uncertainties in Terrestrial Enhanced Weathering. Environ. Sci. Technol. **2022**, 56 (22), 15261–15272. https://doi.org/10.1021/acs.est.2c03163.
(14) Beerling, D. J.; Leake, J. R.; Long, S. P.; Scholes, J. D.; Ton, J.; Nelson, P. N.; Bird, M.; Kantzas, E.; Taylor, L. L.; Sarkar, B.; Kelland, M.; Delucia, E.; Kantola, I.; Müller, C.; Rau, G. H.; Hansen, J. Farming with Crops and Rocks to Address Global Climate, Food and Soil Security. Nature Plants **2018**, 4 (3), 138–147. https://doi.org/10.1038/s41477-018-0108-y.
(15) Goll, D. S.; Ciais, P.; Amann, T.; Buermann, W.; Chang, J.; Eker, S.; Hartmann, J.; Janssens, I.; Li, W.; Obersteiner, M.; Penuelas, J.; Tanaka, K.; Vicca, S. Potential CO2 Removal from Enhanced Weathering by Ecosystem Responses to Powdered Rock. Nature Geoscience **2021**, 14 (8), 545–549. https://doi.org/10.1038/s41561-021-00798-x.
(16) Mühlbauer, A.; Keiner, D.; Breyer, C. Techno-Economic Insights and Deployment Prospects of Permanent Carbon Dioxide Sequestration in Solid Carbonates. Energy Environ. Sci. **2024**, 17 (22), 8756–8775. https://doi.org/10.1039/D4EE03166K.
(17) Keith, D. W.; Holmes, G.; St. Angelo, D.; Heidel, K. A Process for Capturing CO2 from the Atmosphere. Joule **2018**, 2 (8), 1573–1594. https://doi.org/10.1016/j.joule.2018.05.006.
(18) Deutz, S.; Bardow, A. Life-Cycle Assessment of an Industrial Direct Air Capture Process Based on Temperature–Vacuum Swing Adsorption. Nature Energy **2021**, 6, 203–213. https://doi.org/10.1038/s41560-020-00771-9.
(19) Bertagni, M. B.; Calabrese, S.; Cipolla, G.; Noto, L. V.; Porporato, A. Advancing Enhanced Weathering Modeling in Soils: Critical Comparison With Experimental Data. J Adv Model Earth Syst **2025**, 17 (1), e2024MS004224. https://doi.org/10.1029/2024MS004224.
(20) Dupla, X.; Bertagni, M. B.; Grand, S. Three Years of Field Trials Indicate a Sustained Enhanced Rock Weathering Signal with Limited CO_2 Removal. Environ. Sci. Technol. **2025**, 59 (48), 25751–25764. https://doi.org/10.1021/acs.est.5c09820.
(21) Brantley, S. L. Understanding the Lab-Field Discrepancy in Mineral Dissolution From Flasks to Enhanced Rock Weathering. Reviews of Geophysics **2025**, 63 (4), e2025RG000881. https://doi.org/10.1029/2025RG000881.
(22) Clarkson, M. O.; Larkin, C. S.; Swoboda, P.; Reershemius, T.; Suhrhoff, T. J.; Maesano, C. N.; Campbell, J. S. A Review of Measurement for Quantification of Carbon Dioxide Removal by Enhanced Weathering in Soil. Front. Clim. **2024**, 6, 1345224. https://doi.org/10.3389/fclim.2024.1345224.
(23) Holden, F. J.; Davies, K.; Bird, M. I.; Hume, R.; Green, H.; Beerling, D. J.; Nelson, P. N. In-Field Carbon Dioxide Removal via Weathering of Crushed Basalt Applied to Acidic Tropical Agricultural Soil. Science of The Total Environment **2024**, 955, 176568. https://doi.org/10.1016/j.scitotenv.2024.176568.
(24) Harrington, K. J.; Hilton, R. G.; Henderson, G. M. Implications of the Riverine Response to Enhanced Weathering for CO2 Removal in the UK. Applied Geochemistry **2023**, 152, 105643. https://doi.org/10.1016/j.apgeochem.2023.105643.
(25) Zhang, S.; Planavsky, N. J.; Katchinoff, J.; Raymond, P. A.; Kanzaki, Y.; Reershemius, T.; Reinhard, C. T. River Chemistry Constraints on the Carbon Capture Potential of Surficial Enhanced Rock Weathering. Limnology and Oceanography **2022**, 9999, 1–10.
(26) Zhang, S.; Reinhard, C. T.; Liu, S.; Kanzaki, Y.; Planavsky, N. J. A Framework for Modeling Carbon Loss from Rivers Following Terrestrial Enhanced Weathering. Environ. Res. Lett. **2025**, 20 (2), 024014. https://doi.org/10.1088/1748-9326/ada398.
(27) Vienne, A.; Frings, P.; Rijnders, J.; Boito, L.; Hartmann, J.; Niron, H.; Poetra, R.; Estrada, M. P.; Reershemius, T.; Steinwidder, L.; Suhrhoff, T. J.; Vicca, S. Weathering without Realizing Inorganic CO_2 Removal Revealed through Base Cation Monitoring. SOIL **2026**, 12 (1), 421–440. https://doi.org/10.5194/soil-12-421-2026.
(28) Haque, F.; Chiang, Y. W.; Santos, R. M. Risk Assessment of Ni, Cr, and Si Release from Alkaline Minerals during Enhanced Weathering. Open Agriculture **2020**, 5 (1), 166–175. https://doi.org/10.1515/opag-2020-0016.

(29) Dupla, X.; Möller, B.; Baveye, P. C.; Grand, S. Potential Accumulation of Toxic Trace Elements in Soils during Enhanced Rock Weathering. European Journal of Soil Science **2023**, 74 (1). https://doi.org/10.1111/ejss.13343.
(30) Flipkens, G.; Blust, R.; Town, R. M. Deriving Nickel (Ni(II)) and Chromium (Cr(III)) Based Environmentally Safe Olivine Guidelines for Coastal Enhanced Silicate Weathering. Environmental Science and Technology **2021**, 55 (18), 12362–12371. https://doi.org/10.1021/acs.est.1c02974.
(31) Beerling, D. J.; Epihov, D. Z.; Kantola, I. B.; Masters, M. D.; Reershemius, T.; Planavsky, N. J.; Reinhard, C. T.; Jordan, J. S.; Thorne, S. J.; Weber, J.; Val Martin, M.; Freckleton, R. P.; Hartley, S. E.; James, R. H.; Pearce, C. R.; DeLucia, E. H.; Banwart, S. A. Enhanced Weathering in the US Corn Belt Delivers Carbon Removal with Agronomic Benefits. Proc. Natl. Acad. Sci. U.S.A. **2024**, 121 (9), e2319436121. https://doi.org/10.1073/pnas.2319436121.
(32) Vienne, A.; Poblador, S.; Portillo-Estrada, M.; Hartmann, J.; Ijiehon, S.; Wade, P.; Vicca, S. Enhanced Weathering Using Basalt Rock Powder: Carbon Sequestration, Co-Benefits and Risks in a Mesocosm Study With Solanum Tuberosum. Front. Clim. **2022**, 4, 869456. https://doi.org/10.3389/fclim.2022.869456.
(33) Rijnders, J.; Vienne, A.; Vicca, S. Effects of Basalt, Concrete Fines, and Steel Slag on Maize Growth and Toxic Trace Element Accumulation in an Enhanced Weathering Experiment. Biogeosciences **2025**, 22 (12), 2803–2829. https://doi.org/10.5194/bg-22-2803-2025.
(34) Vienne, A.; Newell, J.; Roussard, J.; Doherty, R.; Cox, S. F.; Lyons, G.; Vicca, S. Effects of Basalt and Biochar Addition on Base Cations and Trace Metals in Plants and Soil in an Urban Field Trial. Biogeosciences **2026**, 23 (4), 1681–1695. https://doi.org/10.5194/bg-23-1681-2026.
(35) Bell, D. S.; Epihov, D. Z.; Dupla, X.; Beerling, D. J.; Leake, J. R. Enhanced Rock Weathering in Grassland: Impacts of Basalt Dust on Hay Meadow Soil, Forage, and Floristic Diversity. Science of The Total Environment **2026**, 1038, 181888. https://doi.org/10.1016/j.scitotenv.2026.181888.
(36) Amann, T.; Hartmann, J.; Struyf, E.; De Oliveira Garcia, W.; Fischer, E. K.; Janssens, I.; Meire, P.; Schoelynck, J. Enhanced Weathering and Related Element Fluxes - A Cropland Mesocosm Approach. Biogeosciences **2020**, 17 (1), 103–119. https://doi.org/10.5194/bg-17-103-2020.
(37) Te Pas, E. E. E. M.; Hagens, M.; Comans, R. N. J. Assessment of the Enhanced Weathering Potential of Different Silicate Minerals to Improve Soil Quality and Sequester CO2. Front. Clim. **2023**, 4, 954064. https://doi.org/10.3389/fclim.2022.954064.
(38) Lefebvre, D.; Goglio, P.; Williams, A.; Manning, D. A. C.; de Azevedo, A. C.; Bergmann, M.; Meersmans, J.; Smith, P. Assessing the Potential of Soil Carbonation and Enhanced Weathering through Life Cycle Assessment: A Case Study for Sao Paulo State, Brazil. Journal of Cleaner Production **2019**, 233, 468–481. https://doi.org/10.1016/J.JCLEPRO.2019.06.099.
(39) Zhang, B.; Kroeger, J.; Planavsky, N.; Yao, Y. Techno-Economic and Life Cycle Assessment of Enhanced Rock Weathering: A Case Study from the Midwestern United States. Environmental Science and Technology **2023**, 57 (37), 13828–13837. https://doi.org/10.1021/acs.est.3c01658.
(40) Feng, D.; Hicks, A. Environmental, Human Health, and CO2 Payback Estimation and Comparison of Enhanced Weathering for Carbon Capture Using Wollastonite. Journal of Cleaner Production **2023**, 414, 137625. https://doi.org/10.1016/j.jclepro.2023.137625.
(41) Foteinis, S.; Campbell, J. S.; Renforth, P. Life Cycle Assessment of Coastal Enhanced Weathering for Carbon Dioxide Removal from Air. Environmental Science and Technology **2023**, 57 (15), 6169–6178. https://doi.org/10.1021/acs.est.2c08633.
(42) Kroeger, J.; Zhang, B.; Planavsky, N.; Yao, Y. Analyzing Co-Benefits and Rock Sourcing in Life Cycle and Techno-Economic Assessment of Enhanced Rock Weathering. Environ. Sci. Technol. **2026**, 60 (8), 6215–6226. https://doi.org/10.1021/acs.est.5c14334.
(43) Chen, X.; Wang, X.; Jia, X.; Wang, S.; Tan, R. R.; Wang, B.; Wang, F. Sustainability Analysis of Basalt Enhanced Weathering in China under the Carbon Neutrality Pathway. Environmental Impact Assessment Review **2026**, 119, 108396. https://doi.org/10.1016/j.eiar.2026.108396.
(44) Eufrasio, R. M.; Kantzas, E. P.; Edwards, N. R.; Mercure, J.; Koh, S. C. L.; Beerling, D. J.; Holden, P. B.; Pollitt, H. Environmental and Health Impacts of Atmospheric CO2 Removal by Enhanced Rock Weathering Depend on Nations Energy Mix. communications earth & environment **2022**, 3, 106. https://doi.org/10.1038/s43247-022-00436-3.
(45) Jerden, J.; Mejbel, M.; Filho, A. N. Z.; Carroll, M.; Campe, J. The Impact of Geochemical and Life-Cycle Variables on Carbon Dioxide Removal by Enhanced Rock Weathering: Development and Application of the Stella ERW Model. Applied Geochemistry **2024**, 167, 106002. https://doi.org/10.1016/j.apgeochem.2024.106002.

(46) Breunig, H. M.; Fox, P.; Domen, J.; Kumar, R.; Alves, R. J. E.; Zhalnina, K.; Voigtländer, A.; Deng, H.; Arora, B.; Nico, P. Life Cycle Impact and Cost Analysis of Quarry Materials for Land-Based Enhanced Weathering in Northern California. Journal of Cleaner Production **2024**, 476, 143757. https://doi.org/10.1016/j.jclepro.2024.143757.
(47) Yang, C.; Feng, E. Y. Life Cycle Perspective-Based Modeling Assessment of Ocean Alkalinity Enhancement. Environ. Sci. Technol. **2026**, 60 (5), 4008–4019. https://doi.org/10.1021/acs.est.5c13054.
(48) Power, I. M.; Hatten, V. N. J.; Guo, M.; Schaffer, Z. R.; Rausis, K.; Klyn-Hesselink, H. Are Enhanced Rock Weathering Rates Overestimated? A Few Geochemical and Mineralogical Pitfalls. Front. Clim. **2025**, 6, 1510747. https://doi.org/10.3389/fclim.2024.1510747.
(49) Schiedung, M.; Harrington, K. J.; Dupla, X.; Möller, B.; Facq, E.; Sweere, T.; Don, A.; Hilton, R. G.; Doetterl, S.; Hemingway, J. D. Uncertainties of Enhanced Rock Weathering for Climate-Change Mitigation. Nat Rev Earth Environ **2026**. https://doi.org/10.1038/s43017-026-00761-7.
(50) Frontier. Field weathering portfolio. https://frontierclimate.com/portfolio?pathway=enhanced_weathering.
(51) Beerling, D. J.; Reinhard, C. T.; James, R. H.; Khan, A.; Pidgeon, N.; Planavsky, N. J. Challenges and Opportunities in Scaling Enhanced Weathering for Carbon Dioxide Removal. Nat Rev Earth Environ **2025**, 6 (10), 672–686. https://doi.org/10.1038/s43017-025-00713-7.
(52) Koponen, K.; Braun, J.; Cobo Gutiérrez, S.; Evatt, A.; Golmen, L.; Guillén-Gosálbez, G.; Hamelin, L.; Jenkins, S.; Koljonen, T.; Lee, C.-Y.; Levihn, F.; Paul, A. J.; Perlaviciute, G.; Preston Aragonès, M.; Reiner, D. M.; Similä, L.; Steg, L.; Stoefs, W.; Sunny, N.; Werner, C. Responsible Carbon Dioxide Removals and the EU's 2040 Climate Target. Environ. Res. Lett. **2024**, 19 (9), 091006. https://doi.org/10.1088/1748-9326/ad6d83.
(53) Strefler, J.; Amann, T.; Bauer, N.; Kriegler, E.; Hartmann, J. Potential and Costs of Carbon Dioxide Removal by Enhanced Weathering of Rocks. Environmental Research Letters **2018**, 13 (3), 034010. https://doi.org/10.1088/1748-9326/aaa9c4.
(54) Montserrat, F.; Renforth, P.; Hartmann, J.; Leermakers, M.; Knops, P.; Meysman, F. J. R. Olivine Dissolution in Seawater: Implications for CO2 Sequestration through Enhanced Weathering in Coastal Environments. Environmental Science and Technology **2017**, 51 (7), 3960–3972. https://doi.org/10.1021/acs.est.6b05942.
(55) Flipkens, G.; Fuhr, M.; Fiers, G.; Meysman, F. J. R.; Town, R. M.; Blust, R. Enhanced Olivine Dissolution in Seawater through Continuous Grain Collisions. Geochimica et Cosmochimica Acta **2023**, 359, 84–99. https://doi.org/10.1016/j.gca.2023.09.002.
(56) Renforth, P.; Pogge von Strandmann, P. A. E.; Henderson, G. M. The Dissolution of Olivine Added to Soil: Implications for Enhanced Weathering. Applied Geochemistry **2015**, 61, 109–118. https://doi.org/10.1016/J.APGEOCHEM.2015.05.016.
(57) Cobo, S. Enhanced Weathering Datasets, 2026. https://doi.org/10.5281/zenodo.16094445.
(58) Buckingham, F.; Henderson, G. M.; Holdship, P.; Renforth, P. Soil Core Study Indicates Limited CO2 Removal by Enhanced Weathering in Dry Croplands in the UK. Applied Geochemistry **2022**, 147, 105482. https://doi.org/10.1016/j.apgeochem.2022.105482.
(59) Kelland, M. E.; Wade, P. W.; Lewis, A. L.; Taylor, L. L.; Sarkar, B.; Andrews, M. G.; Lomas, M. R.; Cotton, T. E. A.; Kemp, S. J.; James, R. H.; Pearce, C. R.; Hartley, S. E.; Hodson, M. E.; Leake, J. R.; Banwart, S. A.; Beerling, D. J. Increased Yield and CO2 Sequestration Potential with the C4 Cereal Sorghum Bicolor Cultivated in Basaltic Rock Dust-Amended Agricultural Soil. Global Change Biology **2020**, 26 (6), 3658–3676. https://doi.org/10.1111/gcb.15089.
(60) Williamson, P.; Wallace, D. W. R.; Law, C. S.; Boyd, P. W.; Collos, Y.; Croot, P.; Denman, K.; Riebesell, U.; Takeda, S.; Vivian, C. Ocean Fertilization for Geoengineering: A Review of Effectiveness, Environmental Impacts and Emerging Governance. Process Safety and Environmental Protection **2012**, 90 (6), 475–488. https://doi.org/10.1016/j.psep.2012.10.007.
(61) Siegel, D. A.; Devries, T.; Doney, S. C.; Bell, T. Assessing the Sequestration Time Scales of Some Ocean-Based Carbon Dioxide Reduction Strategies. Environmental Research Letters **2021**, 16 (10), 104003. https://doi.org/10.1088/1748-9326/ac0be0.
(62) Sullivan, M. R.; Primeau, F. W.; Seo, H.; Camps-Castellà, J.; Inomura, K.; Martiny, A. C. Decoupled Timescales of Organic Carbon and Phosphorus Recycling in the Global Ocean. Proc. Natl. Acad. Sci. U.S.A. **2026**, 123 (8), e2514991123. https://doi.org/10.1073/pnas.2514991123.

(63) Pehl, M.; Schreyer, F.; Luderer, G. Modelling Long-Term Industry Energy Demand and CO_2 Emissions in the System Context Using REMIND (Version 3.1.0). Geoscientific Model Development **2024**, 17 (5), 2015–2038. https://doi.org/10.5194/gmd-17-2015-2024.
(64) Riahi, K.; van Vuuren, D. P.; Kriegler, E.; Edmonds, J.; O'Neill, B. C.; Fujimori, S.; Bauer, N.; Calvin, K.; Dellink, R.; Fricko, O.; Lutz, W.; Popp, A.; Cuaresma, J. C.; KC, S.; Leimbach, M.; Jiang, L.; Kram, T.; Rao, S.; Emmerling, J.; Ebi, K.; Hasegawa, T.; Havlik, P.; Humpenöder, F.; Da Silva, L. A.; Smith, S.; Stehfest, E.; Bosetti, V.; Eom, J.; Gernaat, D.; Masui, T.; Rogelj, J.; Strefler, J.; Drouet, L.; Krey, V.; Luderer, G.; Harmsen, M.; Takahashi, K.; Baumstark, L.; Doelman, J. C.; Kainuma, M.; Klimont, Z.; Marangoni, G.; Lotze-Campen, H.; Obersteiner, M.; Tabeau, A.; Tavoni, M. The Shared Socioeconomic Pathways and Their Energy, Land Use, and Greenhouse Gas Emissions Implications: An Overview. Global Environmental Change **2017**, 42, 153–168. https://doi.org/10.1016/J.GLOENVCHA.2016.05.009.
(65) European Commission - Joint Research Centre - Institute for Environment and Sustainability. International Reference Life Cycle Data System (ILCD) Handbook - General Guide for Life Cycle Assessment - Detailed Guidance; 2010.
(66) Arvidsson, R.; Tillman, A. M.; Sandén, B. A.; Janssen, M.; Nordelöf, A.; Kushnir, D.; Molander, S. Environmental Assessment of Emerging Technologies: Recommendations for Prospective LCA. Journal of Industrial Ecology **2018**, 22 (6), 1286–1294. https://doi.org/10.1111/jiec.12690.
(67) Mutel, C. Brightway: An Open Source Framework for Life Cycle Assessment. The Journal of Open Source Software **2017**, 2 (12), 236. https://doi.org/10.21105/joss.00236.
(68) Sacchi, R.; Terlouw, T.; Siala, K.; Dirnaichner, A.; Bauer, C.; Cox, B.; Mutel, C.; Daioglou, V.; Luderer, G. PRospective EnvironMental Impact asSEment (Premise): A Streamlined Approach to Producing Databases for Prospective Life Cycle Assessment Using Integrated Assessment Models. Renewable and Sustainable Energy Reviews **2022**, 160 (February), 112311. https://doi.org/10.1016/j.rser.2022.112311.
(69) Wernet, G.; Bauer, C.; Steubing, B.; Reinhard, J.; Moreno-Ruiz, E.; Weidema, B. The Ecoinvent Database Version 3 (Part I): Overview and Methodology. International Journal of Life Cycle Assessment **2016**, 21 (9), 1218–1230. https://doi.org/10.1007/s11367-016-1087-8.
(70) Beerling, D. J.; Kantzas, E. P.; Lomas, M. R.; Wade, P.; Eufrasio, R. M.; Renforth, P.; Sarkar, B.; Andrews, M. G.; James, R. H.; Pearce, C. R.; Mercure, J. F.; Pollitt, H.; Holden, P. B.; Edwards, N. R.; Khanna, M.; Koh, L.; Quegan, S.; Pidgeon, N. F.; Janssens, I. A.; Hansen, J.; Banwart, S. A. Potential for Large-Scale CO2 Removal via Enhanced Rock Weathering with Croplands. Nature **2020**, 583 (7815), 242–248. https://doi.org/10.1038/s41586-020-2448-9.
(71) Tu, Y.; Rafols, R.; Xu, Y.; Butler, N.; Ababneh, L.; Tao, F.; Ramanathan, V.; Houlton, B. Z.; Liao, C. Scaling up Enhanced Rock Weathering for Equitable Climate Change Mitigation. Commun. Sustain. **2026**, 1 (1), 32. https://doi.org/10.1038/s44458-026-00034-w.
(72) Levasseur, A.; Lesage, P.; Margni, M.; Deschěnes, L.; Samson, R. Considering Time in LCA: Dynamic LCA and Its Application to Global Warming Impact Assessments. Environmental Science and Technology **2010**, 44 (8), 3169–3174. https://doi.org/10.1021/es9030003.
(73) Huijbregts, M. A. J.; Steinmann, Z. J. N.; Elshout, P. M. F.; Stam, G.; Verones, F.; Vieira, M. D. M.; Hollander, A.; Zijp, M.; van Zelm, R. ReCiPe 2016 v1.1. A Harmonized Life Cycle Impact Assessment Method at Midpoint and Endpoint Level. Report I: Characterization.; National Institute for Public Health and the Environment, 2017.
(74) Schulte-Uebbing, L.; De Vries, W. Global-scale Impacts of Nitrogen Deposition on Tree Carbon Sequestration in Tropical, Temperate, and Boreal Forests: A Meta-analysis. Global Change Biology **2018**, 24 (2). https://doi.org/10.1111/gcb.13862.
(75) Huijbregts, M. A. J.; Struijs, J.; Goedkoop, M.; Heijungs, R.; Jan Hendriks, A.; Van De Meent, D. Human Population Intake Fractions and Environmental Fate Factors of Toxic Pollutants in Life Cycle Impact Assessment. Chemosphere **2005**, 61 (10), 1495–1504. https://doi.org/10.1016/j.chemosphere.2005.04.046.
(76) Bourg, A. C. M.; Loch, J. P. G. Mobilization of Heavy Metals as Affected by pH and Redox Conditions. In Biogeodynamics of Pollutants in Soils and Sediments; 1995; pp 87–102. https://doi.org/10.1007/978-3-642-79418-6_4.
(77) Anda, M. Cation Imbalance and Heavy Metal Content of Seven Indonesian Soils as Affected by Elemental Compositions of Parent Rocks. Geoderma **2012**, 189–190, 388–396. https://doi.org/10.1016/j.geoderma.2012.05.009.

(78) Alloway, B. J. Heavy Metals in Soils. Trace Metals in Metalloids and Soils and Their Bioavailability.; Alloway, B. J., Trevor, J. T., Eds.; Springer, 2013; Vol. 22.
(79) Wang, H.; Li, X.; Chen, Y.; Li, Z.; Hedding, D. W.; Nel, W.; Ji, J.; Chen, J. Geochemical Behavior and Potential Health Risk of Heavy Metals in Basalt-Derived Agricultural Soil and Crops: A Case Study from Xuyi County, Eastern China. The Science of the total environment **2020**, 729, 139058. https://doi.org/10.1016/j.scitotenv.2020.139058.
(80) World Heath Organization. Global health estimates: Leading causes of DALYs. https://www.who.int/data/gho/data/themes/mortality-and-global-health-estimates/global-health-estimates-leading-causes-of-dalys (accessed 2024-11-19).
(81) Madankan, M.; Kantzas, E. P.; Espinosa, R. M. E.; Vetter, S. H.; Koh, L.; Smith, P.; Beerling, D. J.; Renforth, P. Larger Rock Extraction Sites Could Improve the Efficiency of Enhanced Rock Weathering in the United Kingdom. Commun Earth Environ **2025**, 6 (1), 666. https://doi.org/10.1038/s43247-025-02656-9.
(82) Fischer, H. A History of the Central Limit Theorem: From Classical to Modern Probability Theory; Springer: New York, NY, 2011. https://doi.org/10.1007/978-0-387-87857-7.
(83) Deng, H.; Sonnenthal, E.; Arora, B.; Breunig, H.; Brodie, E.; Kleber, M.; Spycher, N.; Nico, P. The Environmental Controls on Efficiency of Enhanced Rock Weathering in Soils. Sci Rep **2023**, 13 (1), 9765. https://doi.org/10.1038/s41598-023-36113-4.
(84) Kanzaki, Y.; Planavsky, N. J.; Zhang, S.; Jordan, J.; Suhrhoff, T. J.; Reinhard, C. T. Soil Cation Storage Is a Key Control on the Carbon Removal Dynamics of Enhanced Weathering. Environ. Res. Lett. **2025**, 20 (7), 074055. https://doi.org/10.1088/1748-9326/ade0d5.
(85) Cipolla, G.; Calabrese, S.; Porporato, A.; Noto, L. V. Effects of Precipitation Seasonality, Irrigation, Vegetation Cycle and Soil Type on Enhanced Weathering - Modeling of Cropland Case Studies across Four Sites. Biogeosciences **2022**, 19 (16), 3877–3896. https://doi.org/10.5194/bg-19-3877-2022.
(86) Raudsepp, M. J.; Wilson, S.; Tutolo, B. M. The Fate of CO2, Ca, and Mg after Terrestrial Rock Weathering. Geology **2025**, 53 (11), 904–908. https://doi.org/10.1130/G53354.1.
(87) Finlay, R. D.; Mahmood, S.; Rosenstock, N.; Bolou-Bi, E. B.; Köhler, S. J.; Fahad, Z.; Rosling, A.; Wallander, H.; Belyazid, S.; Bishop, K.; Lian, B. Reviews and Syntheses: Biological Weathering and Its Consequences at Different Spatial Levels – from Nanoscale to Global Scale. Biogeosciences **2020**, 17 (6), 1507–1533. https://doi.org/10.5194/bg-17-1507-2020.
(88) Li, C.; Kang, S.; Gao, Y. Rethinking CO_2 Removal Efficiency in Enhanced Rock Weathering. Environ. Sci. Technol. **2025**, 59 (18), 8878–8880. https://doi.org/10.1021/acs.est.5c03802.
(89) Ooka, M.; Zhao, J.; Zhang, L.; Huang, R.; Sakamuru, S.; TeKrony, C.; Hsieh, J.-H.; Collins, B. J.; Dunnick, J. K.; Dixon, D.; Xia, M. Profiling of Environmental Mixtures Containing Metals for Their Toxicity Pathways and Mechanism of Action. Environ. Sci. Technol. **2025**, 59 (10), 4778–4787. https://doi.org/10.1021/acs.est.4c07995.
(90) Fest, E. P. M. J.; Temminghoff, E. J. M.; Griffioen, J.; Van Riemsdijk, W. H. Proton Buffering and Metal Leaching in Sandy Soils. Environ. Sci. Technol. **2005**, 39 (20), 7901–7908. https://doi.org/10.1021/es0505806.
(91) Sharma, N.; Wang, Z.; Catalano, J. G.; Giammar, D. E. Dynamic Responses of Trace Metal Bioaccessibility to Fluctuating Redox Conditions in Wetland Soils and Stream Sediments. ACS Earth Space Chem. **2022**, 6 (5), 1331–1344. https://doi.org/10.1021/acsearthspacechem.2c00031.

Delayed climate benefits and toxicity risks could hinder the sustainable deployment of enhanced weathering

Supporting Information

Selene Cobo[1]* and Gonzalo Guillén-Gosálbez[2]

[1]Department of Chemical and Biomolecular Engineering, University of Cantabria, Spain

[2]Department of Chemistry and Applied Biosciences, Institute for Chemical and Bioengineering, ETH Zürich, Switzerland.

*cobos@unican.es

This document provides additional information on the methodology, models, assumptions, limitations, and results described in the main manuscript.

Table of contents

1. Nomenclature

We define these main sets:
D ≔ {*d* | *d* ∈ Enhanced weathering datasets}
E ≔ {*e* | *e* ∈ Endpoint impact categories}
EC ≔ {*ec* | *ec* ∈ Environmental compartments}
L ≔ {*l* | *l* ∈ Locations}
M ≔ {*m* | *m* ∈ Midpoint impact categories}
N ≔ {*n* | *n* ∈ Rock types}
S ≔ {*s* | *s* ∈ Elementary flows}
T ≔ {*t* | *t* ∈ Number of years after the rock application}
T^P ≔ {t^p | t^p ∈ Number of years after pulse emission}
Y ≔ {*y* | *y* ∈ Years of rock application}

We also define the following subsets:
J ≔ {*s* | *s* Greenhouse gases}
ME ≔ {*s* | *s* Metals}

Table S1. Parameters and variables used to estimate the greenhouse gas removal efficiency and health and ecosystem impacts.

Symbol	Description	Unit
$\boldsymbol{a^0}$	CO_2 fraction that remains in the atmosphere for an infinite number of years after a pulse emission	–
$\boldsymbol{a^g}$	CO_2 fraction transferred to carbon sink *g* an infinite number of years after a pulse emission.	–
$\boldsymbol{AGWP^{TH}_{CO_2}}$	Absolute global warming potential of CO_2 over a 100-year period	W·year/m^2/kg
$\boldsymbol{AGWP^{TH'}_{s,t}}$	Absolute global warming potential of greenhouse gas *s* emitted or removed in year *t* and quantified over period TH'	W·year/m^2/kg
$\boldsymbol{C_{s,t^p}}$	Fraction of greenhouse gas *s* that remains in the atmosphere t^p years after being emitted	–
$\boldsymbol{CDR_{s,ec,t,y}}$	Gross amount of CO_2 removed from the atmosphere in year *t* after deployment in year *y*	kg/functional unit[a]
$\boldsymbol{CF^{MID}_{m,s,ec,t}}$	Characterization factor quantifying the impacts of elementary flow *s* emitted to environmental compartment *ec* occurring *t* years after rock application in terms of midpoint impact category *m*	unit of midpoint impact[b]/unit of elementary flow[c]
$\boldsymbol{DF^{END}_{m,e}}$	Factor converting midpoint impact *m* to endpoint impact *e*	unit of endpoint impact[d]/unit of midpoint impact[b]
$\boldsymbol{GGR\eta_{t,y}}$	Greenhouse gas removal efficiency *t* years after deployment in year *y*	–

[a] Functional unit: gross geochemical removal of 100 Mt CO_2 in one year.
[b] Unit depends on the midpoint impact category (e.g., kg$PM_{2.5}$ for fine particulate matter formation).
[c] Unit depends on the type of elementary flow (e.g., m^2 for land).
[d] Unit depends on the endpoint impact category (e.g., DALY for human health).

Symbol	Description	Unit
$\boldsymbol{GHG_{s,ec,t,y}}$	Gross amount of greenhouse gas *s* emitted to the atmosphere in year *t* after deployment in year *y*	kg/functional unit[a]
$\boldsymbol{GWP_{s,t}}$	Global warming potential of greenhouse gas *s* emitted in year *t*	$kgCO_2eq/kg$
$\boldsymbol{I_{e,y}^{END}}$	Endpoint impact *e* in year *y*	unit of endpoint impact[d]/functional unit[a]
$\boldsymbol{NR_{s,ec,t,y}}$	Amount of natural resource *s* extracted from environmental compartment *ec* in year *t* after rock application in year *y*	unit of elementary flow[c]/functional unit[a]
$\boldsymbol{P_{s,ec,t,y}}$	Amount of pollutant *s* (excluding greenhouse gases) emitted to environmental compartment *ec* in year *t* after rock application in year *y*	unit of elementary flow[c]/functional unit[a]
$\boldsymbol{PEF_{s,ec,t,y}}$	Amount of elementary flow *s* prevented from being exchanged with environmental compartment *ec* in year *t* after rock application in year *y*	unit of elementary flow[c]/functional unit[a]
$\boldsymbol{Q_{s,ec,t,y}}$	Amount of elementary flow *s* emitted to environmental compartment *ec* in year *t* after rock application in year *y*	unit of elementary flow[c]/functional unit[a]
$\boldsymbol{RF_s}$	Radiative forcing of greenhouse gas *s*	$W/m^2/kg$
$\boldsymbol{t}$	Number of years after deployment	year
$\boldsymbol{t^p}$	Number of years after pulse emission	year
$\boldsymbol{\tau^g}$	Lifetime of CO_2 perturbation in carbon sink *g*	year
$\boldsymbol{\tau_s}$	Lifetime of greenhouse gas *s* in the atmosphere	year
$\boldsymbol{TF_{s,ec}^{C}}$	Toxicity factor quantifying the carcinogenic toxicity effects of metal *s* emitted to environmental compartment *ec*	DALY/kg
$\boldsymbol{TF_{s,ec}^{NC}}$	Toxicity factor quantifying the non-carcinogenic toxicity effects of metal *s* emitted to environmental compartment *ec*	DALY/kg
$\boldsymbol{TH}$	Time horizon	year
$\boldsymbol{TH'}$	Time horizon spanning from the year of the emission to the final year of TH	year

Table S2. Parameters and variables used in the enhanced weathering models.

Symbol	Description	Unit
$\boldsymbol{A}$	Considered time interval	year
$\boldsymbol{C_n^{ALK}}$	Alkalinity concentration in rock *n*	mol/kg
$\boldsymbol{CDR_{d,l,n,t}}$	CO_2 removed during year *t* after a single rock application, dependent on the type of data *d*, location *l* and rock *n*	kg
$\boldsymbol{CDR^{FU}}$	Functional unit: gross amount of CO_2 removed via enhanced weathering reactions within one year	kg/year
$\boldsymbol{Ea_n}$	Activation energy for the weathering of rock *n*	J/mol
$\boldsymbol{P_n}$	Theoretical CO_2 removal potential of rock *n*	$kgCO_2$/kg rock
$\boldsymbol{MM^{CO_2}}$	CO_2 molecular mass	kg/mol
$\boldsymbol{R}$	Universal gas constant	J/mol/K
$\boldsymbol{RM^0_{d,l,n}}$	Mass of rock that must be initially applied to the soil, dependent on the type of data *d*, location *l* and rock *n*	kg
$\boldsymbol{RM^A_{d,l,n}}$	Mass of rock applied annually after the initial year of deployment, dependent on the type of data *d*, location *l* and rock *n*	kg/year
$\boldsymbol{RM^{CUM}_{d,l,n,t}}$	Amount of rock weathered from the time of application until the end of year *t*, dependent on the type of data *d*, location *l* and rock *n*	kg
$\boldsymbol{RM^{UN}_{d,l,n,t}}$	Remaining unweathered rock *t* years after application, dependent on the type of data *d*, location *l* and rock *n*	kg
$\boldsymbol{spy}$	Number of seconds in a year	s/year
$\boldsymbol{SSA_{d,n}}$	Specific surface area, dependent on the type of data *d* and rock *n*	m^2/kg
$\boldsymbol{T^R}$	Reference temperature used for the normalization of rock weathering and alkalinity dissolution rates in this study	K
$\boldsymbol{T^0_{d,l,n}}$	Temperature reported in the literature for rock weathering and alkalinity dissolution rates, dependent on the type of data *d*, location *l* and rock *n*	K
$\boldsymbol{w}$	CO_2 removal efficiency factor (moles of CO_2 removed per mole of alkalinity released)	–
$\boldsymbol{WR^{ALK_{T^R}}_{d,l,n}}$	Alkalinity dissolution rate at 15 °C, dependent on the type of data *d*, location *l* and rock *n*	mol/m^2/s
$\boldsymbol{WR^{ALK_{T^0}}_{d,l,n}}$	Alkalinity dissolution rate reported in the literature at temperature T^0 for type of data *d*, location *l* and rock *n*	mol/m^2/s
$\boldsymbol{WR^{ROCK_{T^R}}_{d,l,n}}$	Rock weathering rate at 15 °C, dependent on the type of data *d*, location *l* and rock *n*	kg/m^2/s
$\boldsymbol{WR^{ROCK_{T^0}}_{d,l,n}}$	Rock weathering rate reported in the literature at temperature T^0, dependent on the type of data *d*, location *l* and rock *n*	kg/m^2/s

2. Methods

Here we describe how we estimated the greenhouse gas removal efficiency and the health and ecosystem impacts.

2.1 Greenhouse gas removal efficiency

The greenhouse gas removal efficiency defined in Equation E1 of the main manuscript is estimated with the time-dependent Global Warming Potential (GWP) of greenhouse gas *s* emitted or removed in year *t*, expressed in kg CO_2eq per kg of gas ($GWP_{s,t}$, Equation SE1).

$GWP_{s,t}$ is derived from the methodology proposed in [1] to estimate dynamic characterization factors for variable time horizons. With this method, the greenhouse gases emitted (or removed) *t* years after the initial deployment will only contribute to (or prevent) global warming during a time horizon TH' contained within the studied 100-year time horizon (TH), estimated as $TH' = TH - t$.

$GWP_{s,t}$ is computed as the ratio between the absolute GWP of greenhouse gas *s* emitted or removed in year *t* and quantified over period TH' ($AGWP_{s,t}^{TH'}$, Equation SE2), and the absolute GWP of CO_2 over a 100-year period ($AGWP_{CO_2}^{TH}$, Equation SE3), both expressed in W·year/m^2/kg. These are calculated with the radiative forcing of the specific greenhouse gas (RF_s, in W/m^2/kg, taken from [2]) and the share of CO_2 (Equation SE4) and other greenhouse gases (Equation SE5) that remains in the atmosphere t^p years after a pulse emission (C_{s,t^p}). The parameters needed to estimate C_{s,t^p} (a_0, a_g, τ_g and τ_s) are taken from [3]

$$GWP_{s,t} = \frac{AGWP_{s,t}^{TH'}}{AGWP_{CO_2}^{TH}} \quad \forall\, s \in J, t \in T \tag{SE1}$$

$$AGWP_{s,t}^{TH'} = \int_{t^p=0}^{t^p=TH-t} RF_s \cdot C_{s,t^p} \cdot dt^p \quad \forall\, s \in J, t \in T \tag{SE2}$$

$$AGWP_{CO_2}^{TH} = \int_{t^p=0}^{t^p=TH} RF_s \cdot C_{s,t^p} \cdot dt^p \quad \forall\, s = CO_2 \tag{SE3}$$

$$C_{s,t^p} = a^0 + \sum_{g=1}^{3} a^g \cdot e^{-\frac{t^p}{\tau^g}} \quad \forall\, s = CO_2, t^p \in T^P \tag{SE4}$$

$$C_{s,t^p} = e^{-\frac{t^p}{\tau_s}} \quad \forall\, s \neq CO_2, t^p \in T^P \tag{SE5}$$

Figure S1 illustrates how the dynamic dimension of the greenhouse gas emissions is accounted for in a hypothetical scenario where 1 tonne (t) carbon dioxide removal (CDR) and 0.5 t CO_2eq occur at $t = 0$, and 0.5 t CO_2 are additionally removed after 25 years. The curves in the figure represent the instantaneous radiative forcing of the CDR and emission pulses, i.e., the global warming impacts (expressed in W·year/m^2) are estimated as the sum of the colored areas between the curves and the x axis, which are negative for CDR and positive for CO_2 emissions. As the figure shows, the prevented impacts of the second CDR pulse are only quantified for the last 75 years of the considered 100-year timeframe and are therefore lower than the prevented

impacts of the pulse emission of the same magnitude occurring at the beginning of the time horizon.

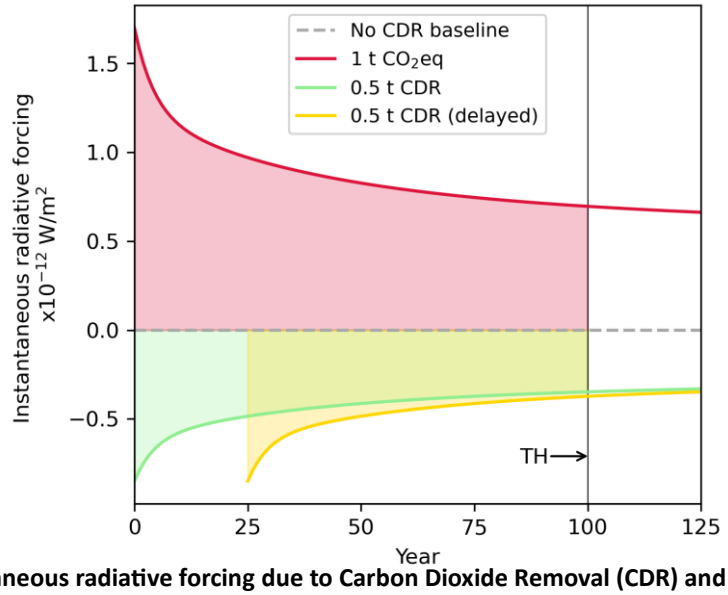

Fig. S1. **Instantaneous radiative forcing due to Carbon Dioxide Removal (CDR) and greenhouse gas pulse emissions.** The areas under the curves represent the global warming impacts (in W·year/m^2) over a 100-year time horizon (TH).

2.2 Health and ecosystem impacts

We estimated the impacts of our scenarios on human health and ecosystems with the ReCiPe 2016[4] impact assessment method, which establishes a linear relationship between the damage to these endpoint areas of protection and the elementary flows (natural resources and emissions) in the life cycle inventories.

We calculated the impacts at the midpoint level–those related to environmental mechanisms such as particulate matter formation or land use–by multiplying the amount of elementary flow *s* exchanged with the environment due to the rock application in year *y* ($Q_{s,ec,t,y}$) by the elementary flow's characterization factor for midpoint impact category *m* ($CF^{MID}_{m,s,ec,t}$). Notably, when the health and ecosystem damage linked to the global warming midpoint impact category are quantified, the characterization factor $CF^{MID}_{m,s,ec,t}$ equals the $GWP_{s,t}$ defined in Equation SE1.

Consistent with our goal of quantifying the impacts of CDR in year *y* (2030 or 2050), we only consider the elementary flows happening during that year, i.e., the initial year of the considered time horizon ($t = 0$). Since CDR happens progressively as rock particles weather, emissions occurring after the initial year of rock application are allocated to subsequent CDR.

We applied a factor $DF^{END}_{m,e}$ to transform midpoint impacts into impacts on the endpoint area of protection *e* (damage to human health or ecosystems). As Equation SE6 indicates, we calculate the endpoint impacts of the CDR occurring in year *y*, $I^{END}_{e,y}$, as the sum of the endpoint impacts quantified over the selected time horizon.

$$I_{e,y}^{END} = \sum_{s \in S} \sum_{ec \in EC} \sum_{m \in M} Q_{s,ec,t,y} \cdot CF_{m,s,ec,t}^{MID} \cdot DF_{m,e}^{END} \quad \forall\, t = 0, e \in E, y \in Y \tag{SE6}$$

The elementary flows $Q_{s,ec,t,y}$ (defined in Equation SE7) are those exchanged with the environment throughout the rock supply chains, and include the removed CO_2 ($CDR_{s,ec=air,t,y}$), greenhouse gas emissions ($GHG_{s,ec=air,t,y}$), other pollutants ($P_{s,ec,t,y}$) and natural resources ($NR_{s,ec,t,y}$), plus the elementary flows prevented from being emitted or extracted as a result of the fertilization effects associated with the released phosphorus. Note that the values of the elementary flows removed or prevented ($CDR_{s,ec=air,t,y}$ and $PEF_{s,ec,t,y}$) are ≤0.

$$Q_{s,ec,t,y} = CDR_{s,ec=air,t,y} + GHG_{s,ec=air,t,y} + P_{s,ec,t,y} + NR_{s,ec,t,y} + PEF_{s,ec,t,y} \quad \forall\, s \in S,\ ec \in EC, t \in T, y \in Y \tag{SE7}$$

The ReCiPe 2016 impact assessment method handles uncertainty by defining three cultural perspectives that group different sources of uncertainty and value choices. While the main manuscript focuses primarily on the hierarchist middle-ground perspective, toxicity impacts calculated for alternative perspectives are provided in the Supporting results section. Cultural perspectives are defined as follows:

- Individualist (20-year time horizon). It quantifies short-term impacts based on a very high level of evidence and technological optimism regarding human adaptation. Humans are only exposed to metals through drinking water and air.
- Hierarchist (100-year time horizon). The considered timeframe and plausibility of impact mechanisms are based on the scientific consensus. It considers all exposure routes.
- Egalitarian (infinite time horizon). It reflects the most precautionary approach for damage modeling, considering all exposure routes.

The metal toxicity factors $TF_{s,ec}^{C}$ and $TF_{s,ec}^{NC}$ in Equation E2 of the main manuscript are calculated as the product of $CF_{m,s,ec,t}^{MID}$ and $DF_{m,e}^{END}$ for the human health (*H*) endpoint and the carcinogenic (*C*) and non-carcinogenic (*NC*) toxicity midpoint impact categories, respectively (Equations SE8 and SE9).

$$TF_{s,ec}^{C} = CF_{m,s,ec,t}^{MID} \cdot DF_{m,e}^{END} \quad \forall\, s \in ME, ec \in EC, m = C, e = H, t = 0 \tag{SE8}$$

$$TF_{s,ec}^{NC} = CF_{m,s,ec,t}^{MID} \cdot DF_{m,e}^{END} \quad \forall\, s \in ME, ec \in EC, m = NC, e = H, t = 0 \tag{SE9}$$

The characterization factors provided by the ReCiPe 2016 method to quantify human toxicity and ecotoxicity are derived from the USES-LCA 2.0[5] model and the USETOX[6] database. These global toxicity factors are directly proportional to the product of fate, exposure, and effect factors, described below.

- Fate factors represent the environmental persistence of a substance, quantified as the marginal change in the dissolved steady state concentration in an environmental compartment due to a marginal emission change[7].
- Exposure factors account for the fraction of a substance in a given environmental compartment that is bioavailable. Human exposure occurs through inhalation or oral uptake (via food or drinking water) and varies across geographical scales. Regional exposure factors are ultimately aggregated into a global, population-weighted average. Notably, dietary ingestion dominates human metal intake in the long term; it accounts for 98.7% and 86.7%

(median) of the intake fractions when metals are emitted to agricultural and natural soils, respectively. For metal emissions to seawater, exposure through food represents 100% of the intake fraction[7]. Specifically, metals accumulate in food products through three mechanisms: 1) crops take up metals from soil, 2) livestock ingest metals in feed, and 3) fish absorb metals from contaminated waters[7]. For ecosystems, exposure factors represent the dissolved fraction of a substance, which is assumed to be bioavailable[6].

- Effect factors quantify the toxicity effects of the emitted substance, derived from human and ecological toxicity data[8].

3. Enhanced weathering models

Next, we summarize the key equations and variables, data sources, and main assumptions and limitations of our models.

3.1 Equations and variables

The enhanced weathering life cycle inventories are estimated with two sets of data (d): experimental (exp) and theoretical (th), differentiating between the rock type *n* (basalt or dunite) and the location *l* of the rock application (inland or coastal).

We used the Arrhenius equation to calculate the alkalinity dissolution and rock weathering rates at a reference temperature T^R of 15 °C ($WR_{d,l,n}^{ALK_{T^R}}$ and $WR_{d,l,n}^{ROCK_{T^R}}$, expressed in mol/m^2/s and kg/m^2/s, respectively) based on the alkalinity dissolution and rock weathering rates ($WR_{d,l,n}^{ALK_{T^0}}$ and $WR_{d,l,n}^{ROCK_{T^0}}$) reported in the literature for temperature $T_{d,l,n}^0$, and considering activation energy (Ea_n) values of 5·10^4 J/mol for basalt[9] and 6.09·10^4 J/mol for dunite[10] (Equations SE10 and SE11). The temperature-normalized results are compiled in Tables 1.3 and 1.4 of the Supporting Data[11].

$$WR_{d,l,n}^{ALK_{T^R}} = WR_{d,l,n}^{ALK_{T^0}} \cdot e^{-\frac{Ea_n}{R}\cdot\left(\frac{1}{T^R}-\frac{1}{T_{d,l,n}^0}\right)} \quad \forall\, d \in exp, l \in L, n \in N \qquad \text{(SE10)}$$

$$WR_{d,l,n}^{ROCK_{T^R}} = WR_{d,l,n}^{ROCK_{T^0}} \cdot e^{-\frac{Ea_n}{R}\cdot\left(\frac{1}{T^R}-\frac{1}{T_{d,l,n}^0}\right)} \quad \forall\, d \in th, l \in L, n \in N \qquad \text{(SE11)}$$

To calculate the mass of rock that must be initially applied to the soil ($RM_{d,l,n}^0$) in the inland and coastal enhanced weathering scenarios based on experimental data, we used Equation SE12, where CDR^{FU} represents the functional unit (i.e., the amount of CO_2 removed within one year, expressed in kg/year), $SSA_{d,n}$ is the rock specific surface area (SSA, m^2/kg), spy is the number of seconds in a year, and MM^{CO_2} is the CO_2 molecular mass (kg/mol).

Previous studies have found that the dissolution of the silicate minerals is the rate limiting step of the weathering reactions[12]; hence, we assumed that the dissolved minerals can immediately react with the dissolved CO_2. We adjusted the stoichiometric CDR (one mole of atmospheric CO_2 reacts with one mole of alkalinity released from the rock) with a CDR efficiency factor (w) of 0.775 (typically between 0.7 and 0.85)[13] to account for the conversion of some bicarbonate anions to carbonate anions, which occurs under conditions of excess alkalinity and releases part of the sequestered CO_2. While prior studies estimate the fraction of rock dissolved with the shrinking core model[12,14], it has been criticized for considering perfect spherical particles rather than highly irregular grains, thereby underestimating the SSA and leading to longer dissolution times[15,16]. Hence, we opt for considering a constant SSA, consistent with previous analyses[15,17].

In the scenarios based on theoretical data, we estimated $RM_{d,l,n}^0$ with Equation SE13, dividing the annual CDR target by the product of the rock fraction that is weathered in one year and the theoretical rock CDR potential P_n (kgCO_2/kg rock), which is based on the rock chemical composition and accounts for the CDR efficiency factor.

$$RM^{0}_{d,l,n} = \frac{|CDR^{FU}|}{WR^{ALK_{TR}}_{d,l,n} \cdot SSA_{d,n} \cdot spy \cdot w \cdot MM^{CO_2}} \; \forall\, d = exp, l \in L, n \in N \quad \text{(SE12)}$$

$$RM^{0}_{d,l,n} = \frac{|CDR^{FU}|}{WR^{ROCK_{TR}}_{d,l,n} \cdot SSA_{d,n} \cdot spy \cdot P_n} \; \forall\, d = th, l \in L, n \in N \quad \text{(SE13)}$$

We use Equation SE14 to estimate the amount of rock that must be applied every year after the initial deployment ($RM^{A}_{d,l,n}$) to maintain a constant annual CDR rate. Since the amount of alkalinity dissolved is directly proportional to the SSA, maintaining a constant CDR rate requires keeping the total rock surface area constant over time. Hence, we assume that the annual rock application equals the mass of rock that weathered during the previous year, estimated with $WR^{ROCK_{TR}}_{d,l,n}$. For scenarios based on experimental data, $WR^{ROCK_{T}}_{d,l,n}$ is calculated with Equation SE15 based on the alkalinity concentration in the rock, C^{ALK}_{n} (mol/kg).

$$RM^{A}_{d,l,n} = RM^{0}_{d,l,n} \cdot WR^{ROCK_{TR}}_{d,l,n} \cdot SSA_{d,n} \cdot spy \; \forall\, d \in D, l \in L, n \in N \quad \text{(SE14)}$$

$$WR^{ROCK_{TR}}_{d,l,n} = \frac{WR^{ALK_{TR}}_{d,l,n}}{C^{ALK}_{n}} \; \forall\, d = exp, l \in L, n \in N \quad \text{(SE15)}$$

To calculate the dynamic CDR profile resulting from a single rock deployment, we use Equations SE16-SE21. These equations describe how as the initially applied rock gradually weathers, the remaining rock available for weathering decreases, thereby lowering the annual CDR.

The amount of CO_2 removed during year *t* after the rock application ($CDR_{d,l,n,t}$, expressed in kg) is initially 0 (Equation SE16). In subsequent years, $CDR_{d,l,n,t}$ is directly proportional to the mass of rock that weathers in that specific year, as estimated by Equations SE17 and SE18 for scenarios based on experimental and theoretical datasets, respectively.

Calculating the latter requires previously computing the cumulative amount of rock weathered from the time of application until the end of year *t* ($RM^{CUM}_{d,l,n,t}$, in kg). This value is set to 0 initially (Equation SE19) and calculated for subsequent years using Equation SE20, which considers the weathering rates reported in the literature and the remaining amount of rock unweathered at the end of the preceding year. The mass of rock that remains unweathered in year *t* after the rock application ($RM^{UN}_{d,l,n,t}$, in kg) is calculated with Equation SE21.

$$CDR_{d,l,n,t} = 0 \;\; \forall\, d \in D, l \in L, n \in N, t = 0 \quad \text{(SE16)}$$

$$CDR_{d,l,n,t} = RM^{UN}_{d,l,n,t-1} \cdot WR^{ALK_{TR}}_{d,l,n} \cdot SSA \cdot spy \cdot A \cdot w \cdot MM^{CO_2} \quad \text{(SE17)}$$
$$\forall\, d = exp, l \in L, n \in N, t > 0$$

$$CDR_{d,l,n,t} = P_n \cdot (RM^{CUM}_{d,l,n,t} - RM^{CUM}_{d,l,n,t-1}) \;\; \forall\, d = th, l \in L, n \in N, t > 0 \quad \text{(SE18)}$$

$$RM^{CUM}_{d,l,n,t} = 0 \;\; \forall\, d \in D, l \in L, n \in N, t = 0 \quad \text{(SE19)}$$

$$RM^{CUM}_{d,l,n,t} = RM^{UN}_{d,l,n,t-1} \cdot WR^{ROCK_{TR}}_{d,l,n} \cdot SSA \cdot spy \cdot A + RM^{CUM}_{d,l,n,t-1} \quad \text{(SE20)}$$
$$\forall\, d \in D, l \in L, n \in N, t > 0$$

$$RM^{UN}_{d,l,n,t} = \; RM^{0}_{d,l,n} - \; RM^{CUM}_{d,l,n,t} \; \forall\, d \in D, l \in L, n \in N, t \in T \quad \text{(SE21)}$$

3.2 Scenario parameters

Table S3 summarizes the key characteristics of the studies upon which the enhanced weathering scenarios were modeled. The parameters derived from these works are described in further detail below.

We modeled two coastal enhanced weathering scenarios based on the total alkalinity dissolution rates derived from laboratory experiments[18,19] where olivine particles were added to the seawater and subjected to continuous rotation movements to simulate the weathering conditions in coastal environments. In [18], experiments were conducted at 17 °C, and olivine particles had an SSA of 0.295 m^2/g and a median size (p_{50}) of 143 µm, with the size below which 80% of particles fall (p_{80}) ≈200 µm. We calculated the amount of dunite applied considering that olivine makes up 90%[20] of the rock, and an alkalinity content of 20.02 mol/kg dunite[18]. In the coastal enhanced weathering scenarios based on experimental data from [18], we assume that all the nickel contained in the applied dunite is released in the year following rock application, consistent with the high nickel dissolution rates reported.

In the scenarios modeled after the experiments described in [19], which were conducted at 15 °C, p_{50} is 136±1 µm, p_{80} equals 186±2 µm, and the SSA is 0.9±0.1 m^2/g. The olivine share in dunite was 90.54%, and the alkalinity content was 23.31 mol/kg dunite. We also considered the nickel dissolution rates provided in both studies[18,19], and assessed how uncertainties in alkalinity and nickel dissolution rates[18,19] (compiled in Tables 1.3 and 1.5 in the Supporting Data[11]) affected our results. In both coastal enhanced weathering scenarios, we considered an application rate of 22 kg/m^2, as in [20]. This corresponds to the largest application rate across the experimental studies simulating inland conditions. It was selected under the assumption that coastal scenarios permit higher application rates because wave action and tidal transport accelerate the movement of rock particles into the marine environment.

The inland scenarios deploying dunite are based on a mesocosm[20] study conducted at ≈15 °C and a laboratory[21] experiment at 19 °C. Weathering rates were estimated from the amount of magnesium initially contained in the rock that is dissolved during the experiments. In the scenario modeled after [20], we derive data from the experimental setup based on fine dunite grains with a 90% olivine content and a magnesium-related alkalinity concentration of 22.04 mol per kg dunite, considering an application rate of 22 kg/m^2 to the soil. The rock particle data are as follows. Dominant particle size class: 25.5 µm, p_{80}: 43.5 µm, SSA: 12.1 m^2/g (range: 11.8–12.5 m^2/g). For the uncertainty analysis, we estimate the range of alkalinity dissolution rates based on the reported alkalinity concentrations at the outlet of the experimental setup.

In the inland scenario based on data from [21], the application rate is 12.9 kg/m^2. The dominant particle size class is 125-212 µm for dunite particles with an SSA of 3.04±0.03 m^2/g, and we estimate a p_{80} of 368 µm. We assume that 90% of the dunite content is olivine, consistent with [20]. The alkalinity content associated with magnesium is 21.31 mol per kg dunite. Our uncertainty analysis considers the reported range of alkalinity dissolution rates. We assume 0.1 g P_2O_5 per kg of rock across all the dunite scenarios[20,21].

The experimental basalt scenarios are based on data from [22] and [23], both considering a rock application rate of 5 kg/m^2. The alkalinity dissolution rates of the basalt scenarios are compiled

in Table 1.3 of the Supporting Data[11]. In the scenarios modeled after data from soil core experiments[22] at an average temperature of 12 °C, the mass of basalt needed is computed with the alkalinity dissolution rates–estimated from the calcium, magnesium and sodium released in the experiments–and the rock alkalinity content (10.4 mol/kg). Here, the dominant particle size class is 63-250 µm (p_{80}≈ 250 µm), the SSA is 9.23 ± 0.076 m^2/g, and the P_2O_5 concentration is 9 g P_2O_5 per kg of basalt. We analyzed the influence of the reported uncertainty in the alkalinity release rate on our results.

The basalt particles in the scenario considering results from a field trial[23] present a grain size p_{80} of 267 µm and an SSA of 1.02±0.014 m^2/g[24]. Since this study does not provide alkalinity dissolution rates, we derived them from the reported CDR over a four-year period at an average temperature of 10.9 °C[25]. We used a value of $5.25 \cdot 10^{-2}$ kg CO_2 per kg basalt to solve Equation SE12 for $WR_{d,l,n}^{ALK_T}$ (range considered for the uncertainty analysis: $3.35 \cdot 10^{-2}$-$7.15 \cdot 10^{-2}$ kg CO_2 per kg basalt). The alkalinity (calcium and magnesium) content in the applied rock is 7.37 mol per kg of basalt, whereas the P_2O_5 concentration is 1.98 g P_2O_5 per kg of basalt[24].

In the theoretical scenarios, we took the rock weathering rates (and their corresponding uncertainty ranges) estimated in [15] (Table 1.4 in the Supporting Data[11]) . We considered the application of 15 kg/m^2 of rock particles with a uniform size of 25 µm and estimated the SSA (1.28 m^2/g) with the power function provided by [15]. We selected this particle size because it corresponds to the lower end of the dominant class sizes across the experimental studies. Since smaller particles present higher SSAs, leading to higher CDR rates, the theoretical scenarios serve as a high-performance benchmark against which the experimental scenarios can be measured. The assumed CDR potential P_n of dunite and basalt is 0.95 and 0.3 kg CO_2 per kg of rock, respectively[15], while the considered P_2O_5 concentration in the theoretical scenarios is 0.1 g per kg of dunite [20,21] and 2.36 g per kg of basalt[26].

We calculated the electricity demand for the rock crushing and grinding operations using the correlation between the particle size and the energy consumption provided in [15]. We assumed an average road transportation distance of 215 km (range: 180-250 km)[27], based on scenarios linking rock extraction sites and croplands in the United Kingdom. Finally, our inventories do not include land occupation or transformation elementary flows in the foreground system because croplands, forestlands and coastal areas continue providing the same services as prior to the rock deployment.

Table S3. Main characteristics of the source studies used for the enhanced weathering scenarios.
Data gaps (in *italics*) were taken from other studies or assumed *(a)* by the authors.

	Experimental data						**Theoretical data**
	Dunite (D)				**Basalt (B)**		**D/B**
	Coastal		Inland		Inland		
	Laboratory	Laboratory	Mesocosm	Laboratory	Mesocosm	Field	–
	Montserrat et al. (2017)[18]	Flipkens et al. (2023)[19]	Amann et al. (2020)[20]	Renforth et al. (2015)[21]	Vienne et al. (2022)[22]	Beerling et al. (2024)[23]	Strefler et al. (2018)[15]
Temperature T^0 (°C)	17	15	15	19	12	10.9[25]	25
p_{80} (µm)	200	186	43.5	368	250	267	*25 (a)*
p_{50} (µm)	143	136	–	–	–	–	*25 (a)*
Dominant class (µm)	–	–	25.5	125-212	63-250	–	*25 (a)*
SSA (m^2/g)	0.295	0.9	12.1	3.04	9.23	1.02	1.28
Alkalinity (mol/kg rock)	20.02	23.21	22.04	21.31	10.4	7.37	25.40 (D), 8.02 (B)
P_2O_5 (g/kg rock)	*0.1*[20,21]	*0.1*[20,21]	0.1	0.1	9	1.98	*0.1*[20,21] (D), 2.36[26] (B)
Application rate (kg/m^2)	*22*[20]	*22*[20]	22	12.9	5	5	15
Initial pH	7.9-8.2	8.2	6.6	7.5[e]	7.72	6.1	7
Soil properties	–	–	Sandy laom	Calcareous	Loamy	Silt loam	–

[e] pH of the control effluent solution used as proxy.

3.3 Main assumptions and limitations

The functional unit–defined as the gross removal of 100 Mt CO_2 in one year–accounts for 26% and 6% of the 2030 and 2050 CDR targets, respectively, within the selected climate change mitigation scenario (SSP2-PkBudg1000, projected with the REMIND 3.5 integrated assessment model[28,29]).

While this value represents a conservative fraction of the theoretical global potential of enhanced weathering (0.35-2.00 Gt CO_2 per year by 2050, according to previous techno-economic analyses[30,31]), other CDR methods are more likely to scale up faster since they are currently better understood and present higher maturity levels[32]. Hence, the functional unit represents an ambitious yet realistic benchmark.

Ideally, the performance of enhanced weathering trials deploying dunite and basalt should be assessed under equal experimental conditions to enable a fair comparison. This was not possible due to the limited body of experimental results reported in the literature. However, the scenarios based on experimental data allowed us to illustrate the performance gap between the theoretical and experimental weathering rates (discussed in the main text).

To estimate the metal emissions to the soil (inland scenarios) and seawater (coastal scenarios), we considered the metal concentrations in basalt reported in [33–35], and took those of dunite from [20] (Tables 1.1 and 1.2 in the Supporting Data[11]). Although some experiments simulating inland enhanced weathering conditions found slower dissolution rates for certain elements relative to the alkaline metals driving CDR[20,21,36], they did not quantify the accumulation of metals in the soil surface, which could be substantial[37]. Furthermore, metals can potentially be released due to changes in the soil pH or redox conditions[38,39], hard to control in an open field. Thus, our uncertainty analysis considered that metals are released from the weathered rocks at rates ranging between 0% (total retention) and 100% (complete mobilization), allocating the impacts of the elementary flows occurring on a given year to that year's CDR.

Moreover, while we consider global toxicity factors, metal bioavailability is highly dependent on the soil conditions[40], and therefore the application of rock particles to specific locations could lead to varying toxicity effects based on site-specific parameters. Toxicity outcomes are also sensitive to assumptions regarding human adaptation; for instance, factoring in the deployment of advanced water potabilization technologies highly efficient at metal removal could decrease the human intake fractions via drinking water.

Our models do not account for the potential emission of fine particulate matter that could occur during grinding processes[16]. However, because the dominant particle size class considered in our scenarios is significantly larger (≥25 μm) than the hazardous threshold considered by the ReCiPe 2016 method (≤2.5 μm), we expect the potential contribution of fine particulates to the total health effects of our scenarios to be minimal.

On the other hand, we consider that the release of phosphorus contributes to biomass fertilization. However, our model does not account for the potential implications of concurrently applying nitrogen fertilizers and rock particles to the soil; while the latter could partially abate the fertilizer-derived N_2O emissions, the weathering could be driven by HNO_3 instead of the dissolved CO_2, undermining the CDR efficiency[41,42]. Furthermore, enhanced weathering could

lead to additional CDR–not quantified here due to data limitations–through an increase in soil organic carbon[43,44], or improved soil structure and water retention[45]. Another limitation of our models is that they do not reflect the potential co-benefits of counteracting soil and ocean acidification[46], as the ReCiPe 2016[4] impact assessment method lacks characterization factors to quantify the alkalinity-induced neutralization effects of enhanced weathering.

Finally, our inventories are based on global market activities, which implies that the deployment of enhanced weathering in specific locations could lead to different results due to differences in the inventory activities such as the electricity mixes.

4. Supporting results

Here we present additional results to complement the discussion in the main manuscript. Figure S2 shows the time-dependent global warming impacts of our scenarios expressed per t of rock deployed. Figure S3 displays the fraction of rock particles weathered over time following the initial application.

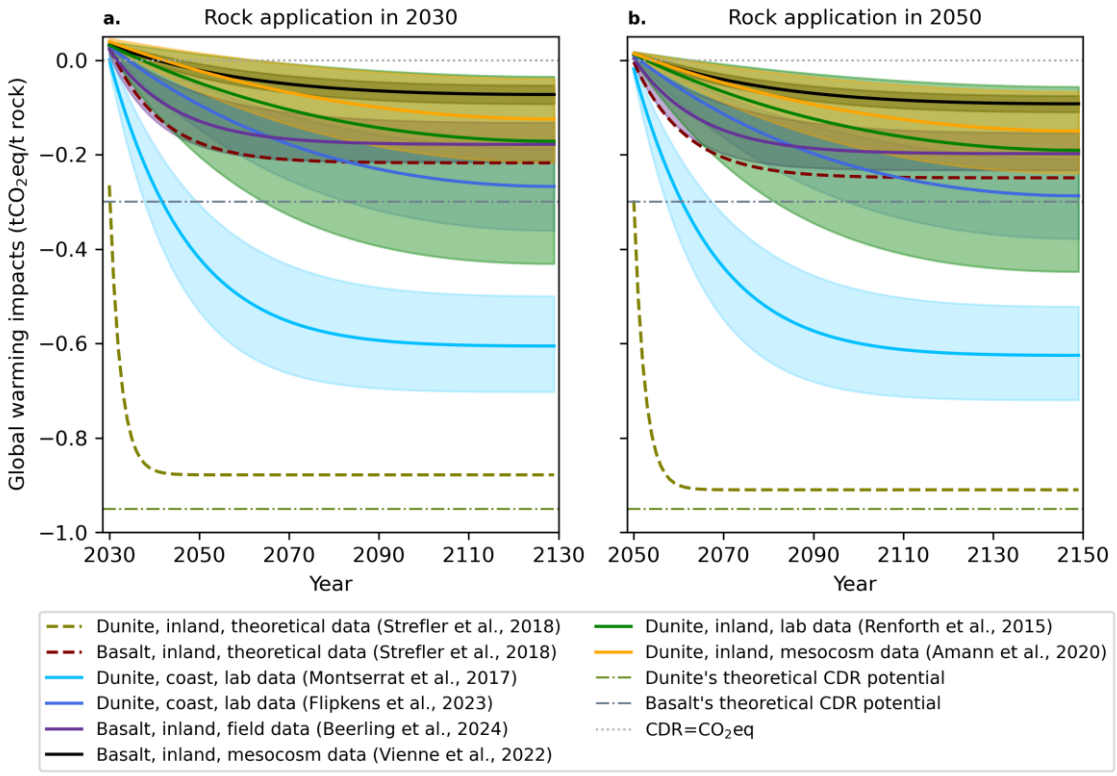

Fig. S2. Evolution of global warming impacts associated with the deployment of 1000 kg of rock at the beginning of the 100-year time horizon, considering experimental[18,20–23,47] and theoretical[15] data for the application of dunite and basalt on coastal and inland environments. The shaded areas represent the uncertainty in the results. **a** Single rock application in 2030. **b** Single rock application in 2050.

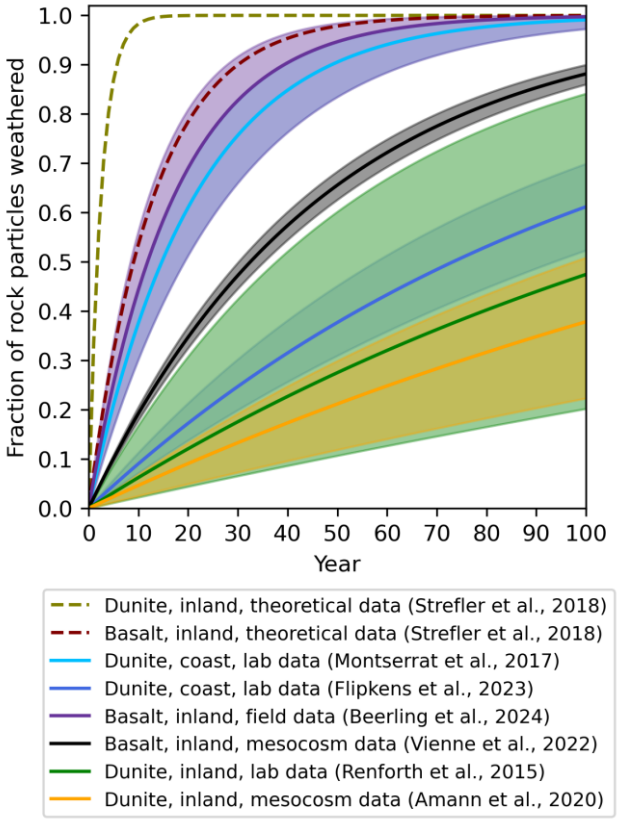

Fig. S3. Fraction of rock particles weathered over 100 years following a single initial application, considering experimental[18–23] and theoretical[15] data for the application of dunite and basalt on coastal and inland environments. The shaded areas represent the uncertainty in the results.

Table S4 shows the number of years required to achieve complete weathering in each scenario.

Table S4. Number of years required to achieve complete weathering in each scenario.

Scenario	Years to achieve complete weathering
Dunite, inland, theoretical data (Strefler et al., 2018)[15]	14
Basalt, inland, theoretical data (Strefler et al., 2018)[15]	70
Dunite, coast, lab data (Montserrat et al., 2017)[18]	113 (91, 147)
Dunite, coast, lab data (Flipkens et al., 2023)[19]	561 (442, 716)
Basalt, inland, field data (Beerling et al., 2024)[23]	91 (64, 148)
Basalt, inland, mesocosm data (Vienne et al., 2022)[22]	249 (231, 270)
Dunite, inland, lab data (Renforth et al., 2015)[21]	824 (288, 2350)
Dunite, inland, mesocosm data (Amann et al., 2020)[20]	1115 (746, 2099)

Figures S4 and S5 illustrate the greenhouse gas removal efficiencies and endpoint (human health and ecosystem) impacts, respectively, for enhanced weathering scenarios aligned with alternative climate change mitigation pathways.

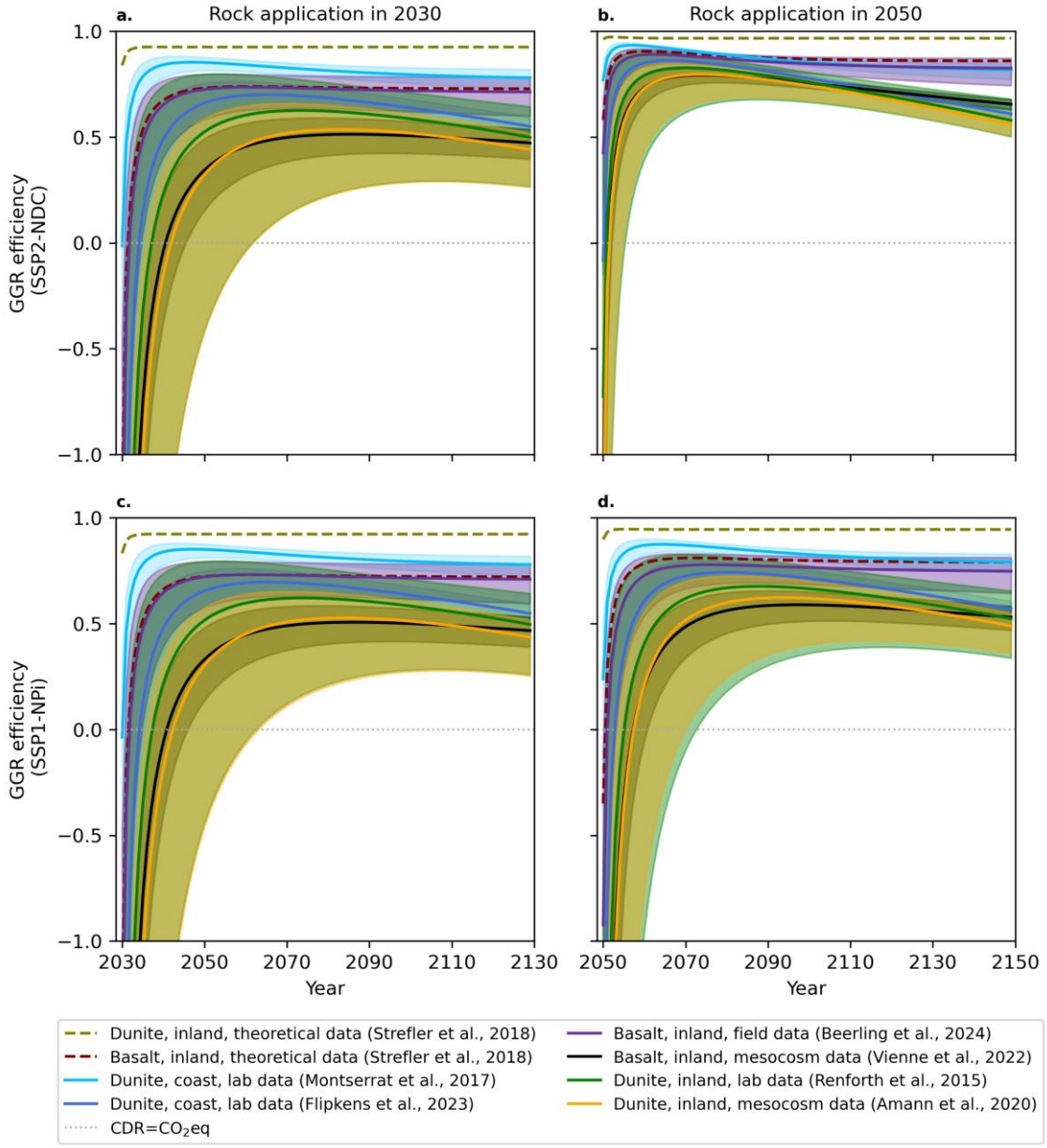

Fig. S4. Evolution of greenhouse gas removal (GGR) efficiencies over 100 years, considering experimental[18–23] and theoretical[15] data for the application of dunite and basalt on coastal and inland environments. The shaded areas represent the uncertainty in the results. **a** Single rock application in 2030, inventory data aligned with SSP2-NDC scenario. **b** Single rock application in 2050, inventory data aligned with SSP2-NDC scenario. **c** Single rock application in 2030, inventory data aligned with SSP1-NPi scenario. **d** Single rock application in 2050, inventory data aligned with SSP1-NPi scenario.

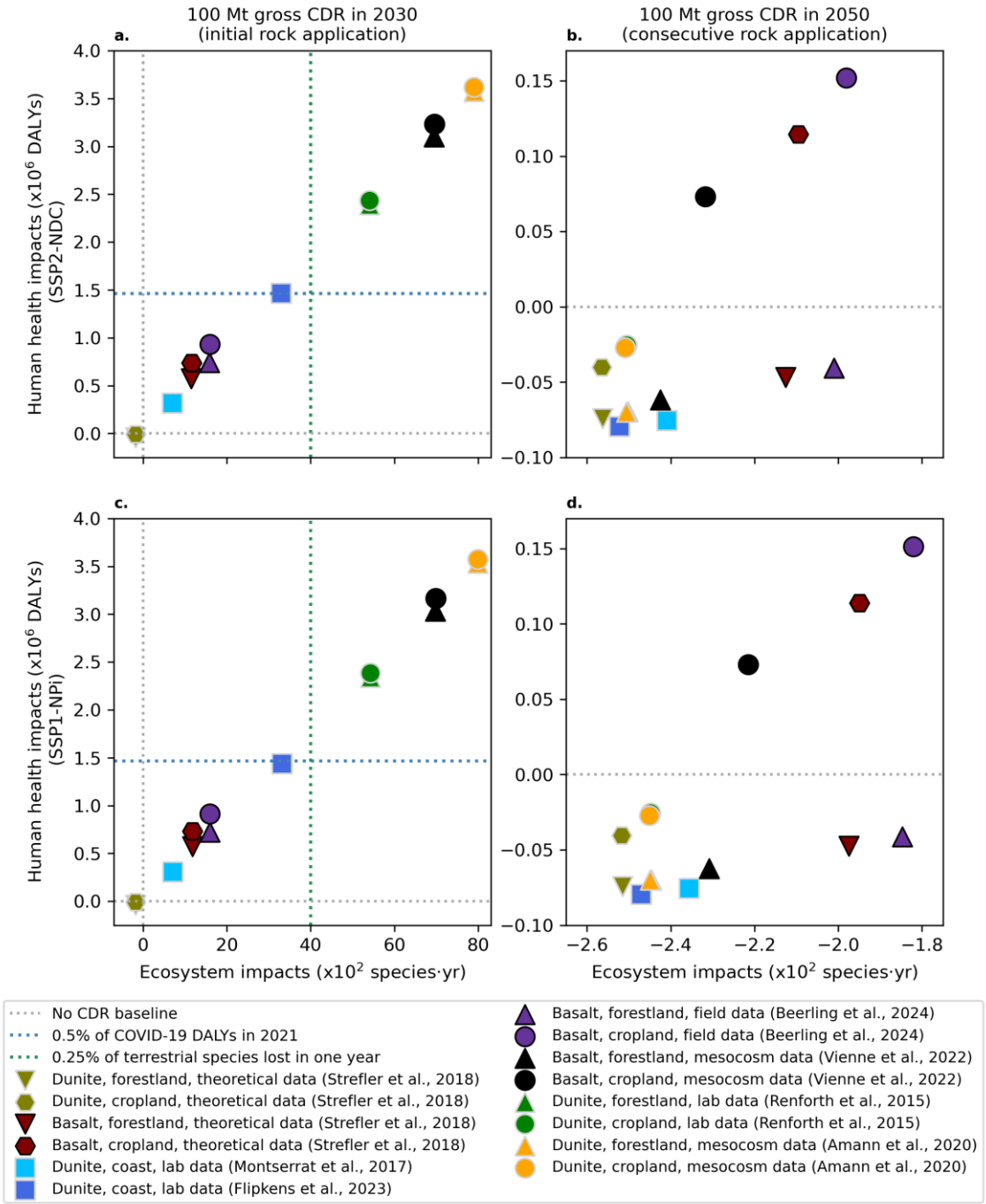

Fig. S5. Human health and ecosystem impacts of removing 100 Mt CO_2 (gross) in 2030 and 2050, considering experimental[18–23] and theoretical[15] data for the application of dunite and basalt on coastal and inland (forestlands and croplands) environments**. a** Rock application in 2030 for the first time, inventory data aligned with SSP2-NDC scenario. **b** Consecutive rock application in 2050, inventory data aligned with SSP2-NDC scenario. **c** Rock application in 2030, inventory data aligned with SSP1-NPi scenario. **d** Consecutive rock application in 2050, inventory data aligned with SSP1-NPi scenario.

Figure S6 depicts the breakdown of health and ecosystem impacts for a coastal enhanced weathering scenario, while Figure S7 shows the disaggregated ecosystem impacts of two inland enhanced weathering scenarios.

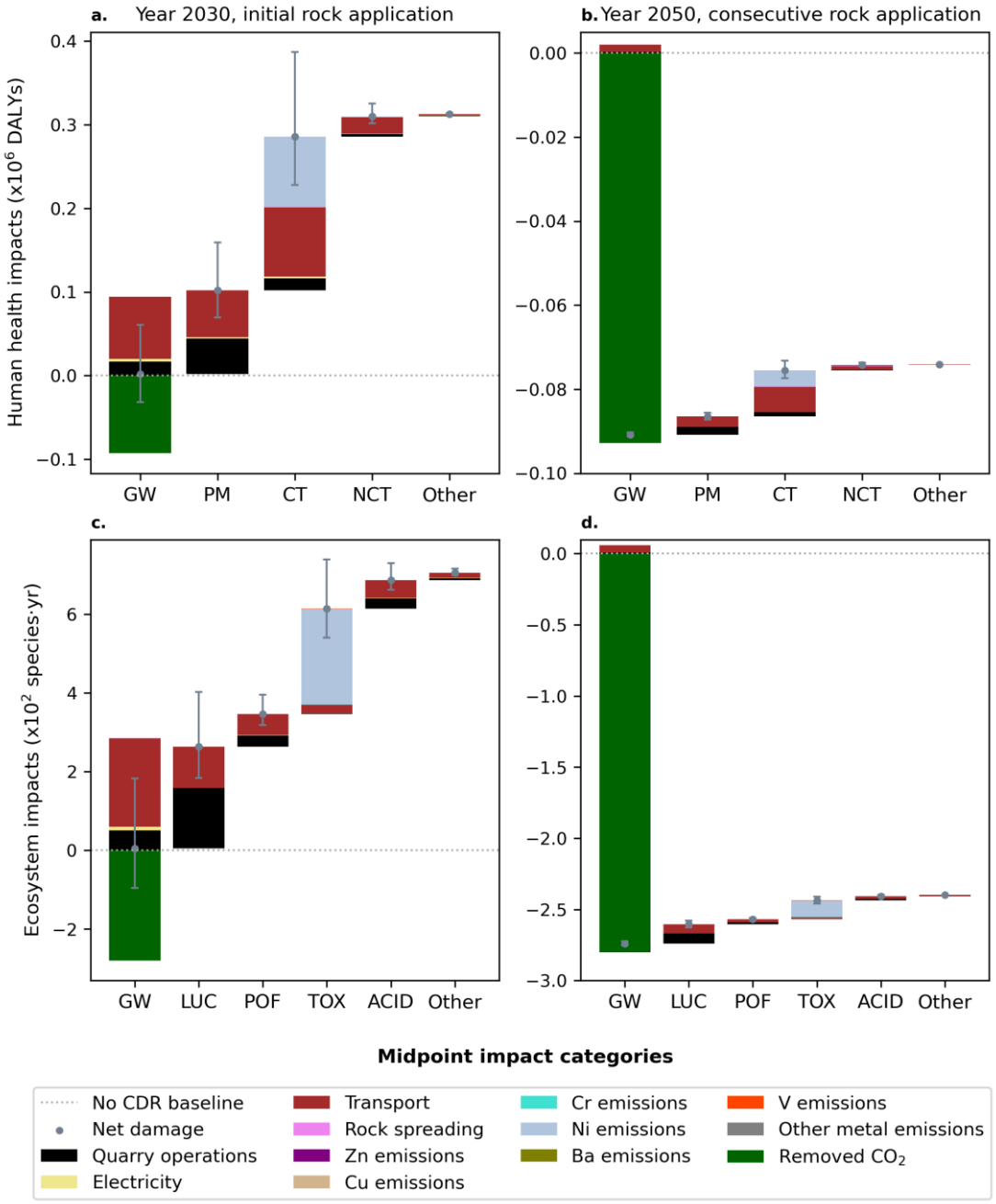

Fig. S6. Health and ecosystem impacts of removing 100 Mt CO_2 (gross) in 2030 and 2050 through coastal enhanced weathering, considering initial rock application in 2030 and consecutive applications in subsequent years. Data from [18]. Error bars represent the uncertainty in the results. Impacts disaggregated by the contribution of i) unit processes and direct emissions, and ii) environmental mechanism leading to health–global warming (GW), fine particulate matter formation (PM), carcinogenic toxicity (CT), non-carcinogenic toxicity (NCT), and others (tropospheric ozone formation, stratospheric ozone depletion, ionizing radiation, and water consumption)–and ecosystem impacts–GW, land-use change (LUC), photochemical ozone formation (POF), ecotoxicity (TOX), terrestrial acidification (ACID) and others (water consumption and eutrophication). **a** Health impacts of dunite application, 2030. **b** Health impacts of dunite application, 2050. **c** Ecosystem impacts of dunite application, 2030. **d** Ecosystem impacts of dunite application, 2050**.**

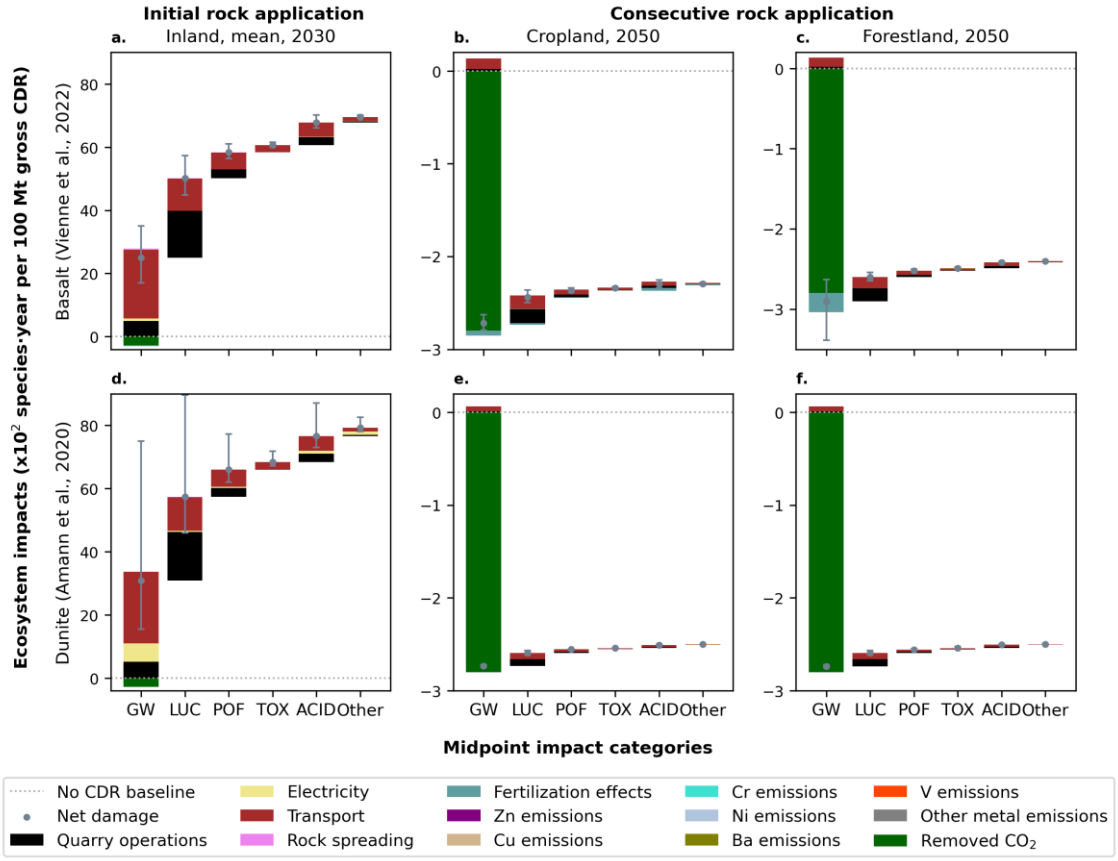

Fig. S7. Ecosystem impacts of removing 100 Mt CO_2 (gross) in 2030 and 2050, considering initial rock application in 2030 and consecutive applications in subsequent years. Data from [20,22]. Error bars represent the uncertainty in the results. Impacts disaggregated by the contribution of i) unit processes and direct emissions, and ii) environmental mechanisms: global warming (GW), land-use change (LUC), photochemical ozone formation (POF), ecotoxicity (TOX), terrestrial acidification (ACID) and others (water consumption and eutrophication). **a** Basalt application to cropland/forestland (mean), 2030. **b** Basalt application to cropland, 2050. **c** Basalt application to forestland, 2050. **d** Dunite application to cropland/forestland (mean), 2030. **e** Dunite application to cropland, 2050. **f** Dunite application to forestland, 2050.

Figure S8 shows the probability distribution of the most impactful metal emissions, derived from the Monte Carlo simulation results. The probability distributions of zinc emissions from basalt (Figure S8a) and dunite (Figure S8c), alongside nickel emissions from dunite (Figure S8d), exhibit a uniform-like, flat-topped shape. By contrast, the probability distribution of nickel emissions from basalt (Figure S8b) features a sharp peak at lower emission values that tapers off into a long right-hand tail.

This distinct shape arises because the literature-reported concentration range for nickel in basalt (72–280 g/t rock) is significantly wider than that of zinc (Tables 1.1 and 1.2 in the Supporting Data), compounding with the other variable parameters in Equation E2 of the main manuscript during the Monte Carlo simulations to mathematically skew the resulting product distribution.

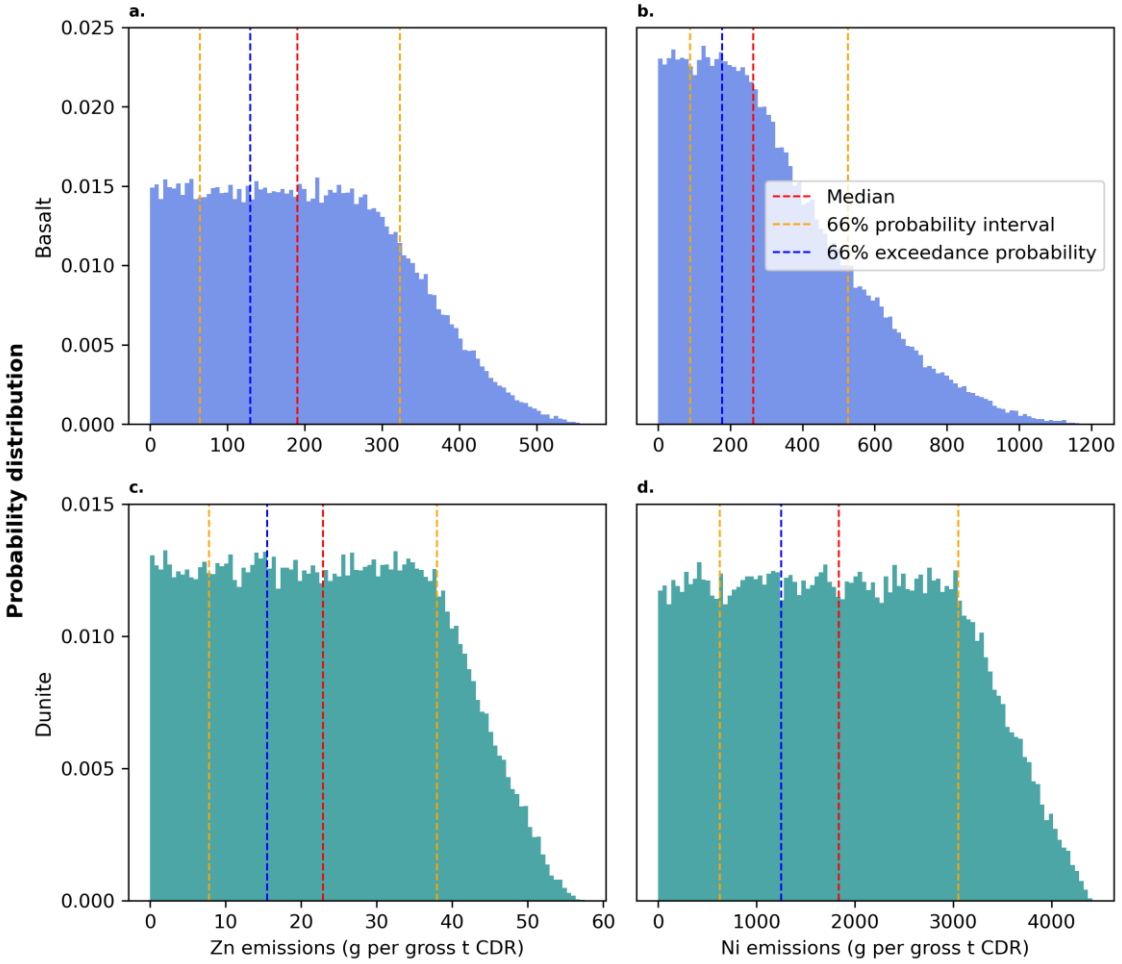

Fig. S8. Probability distributions of selected metal emissions. Data represent Monte Carlo simulation results for **a** Zinc emissions from basalt. **b** Nickel emissions from basalt. **c** Zinc emissions from dunite. **d** Nickel emissions from dunite.

Finally, Figure S9 illustrates the probability distributions of the human toxicity impacts from metal emissions, assuming basalt and dunite application to agricultural soils. The impacts are calculated with the individualistic and egalitarian perspectives of the ReCiPe 2016 method.

Notably, under the individualistic perspective–where exposure via food intake is omitted–the distributional trends observed in Figure 5 of the main manuscript are reversed. Specifically, the concurrent impacts of nickel and other metals in basalt yields a symmetric, single-peaked shape consistent with the central limit theorem[48] (Figure S9a). Conversely, dunite's toxicity impacts become predominantly driven by nickel alone, flattening its profile into a plateau-like shape in accordance with the underlying uniform probability distributions (Figure S9b). The inclusion of all exposure routes results in similarly shaped probability distributions across both the egalitarian (Figures S9c and S9d) and hierarchist (Figure 5) frameworks.

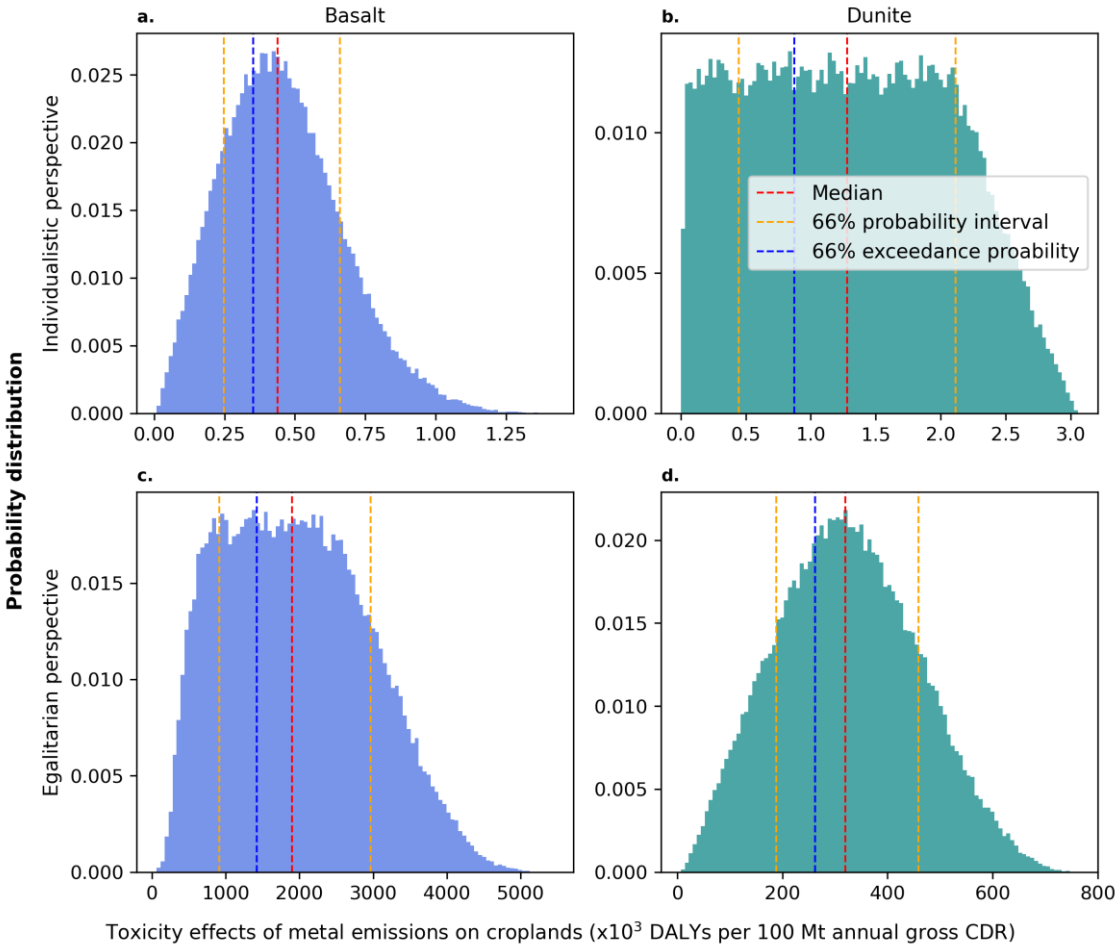

Fig. S9. Probability distributions of toxicity-driven human health impacts due to metal emissions from basalt and dunite to agricultural soil, calculated with the individualist and egalitarian perspectives of the ReCiPe 2016 method. Data represent Monte Carlo simulation results for the annual removal of 100 Mt CO_2 (gross). **a** Basalt, individualist perspective. **b** Dunite, individualist perspective. **c** Basalt, egalitarian perspective. **d** Dunite, egalitarian perspective.

5. References

(1) Levasseur, A.; Lesage, P.; Margni, M.; Deschěnes, L.; Samson, R. Considering Time in LCA: Dynamic LCA and Its Application to Global Warming Impact Assessments. *Environmental Science and Technology* **2010**, *44* (8), 3169–3174. https://doi.org/10.1021/es9030003.

(2) Smith, C.; Nicholls, Z. R. J.; Armour, K.; Collins, W.; Forster, P.; Meinshausen, M.; Palmer, M. D.; Watanabe, M. The Earth's Energy Budget, Climate Feedbacks and Climate Sensitivity-Supplementary Material. In *Climate Change 2021: The Physical Science Basis. Contribution of Working Group I to the Sixth Assessment Report of the Intergovernmental Panel on Climate Change*; 2021.

(3) Millar, J. R.; Nicholls, Z. R.; Friedlingstein, P.; Allen, M. R. A Modified Impulse-Response Representation of the Global near-Surface Air Temperature and Atmospheric Concentration Response to Carbon Dioxide Emissions. *Atmospheric Chemistry and Physics* **2017**, *17* (11), 7213–7228. https://doi.org/10.5194/acp-17-7213-2017.

(4) Huijbregts, M. A. J.; Steinmann, Z. J. N.; Elshout, P. M. F.; Stam, G.; Verones, F.; Vieira, M. D. M.; Hollander, A.; Zijp, M.; van Zelm, R. *ReCiPe 2016 v1.1. A Harmonized Life Cycle Impact Assessment Method at Midpoint and Endpoint Level. Report I: Characterization.*; National Institute for Public Health and the Environment, 2017.

(5) Van Zelm, R.; Huijbregts, M. A. J.; Van De Meent, D. USES-LCA 2.0-a Global Nested Multi-Media Fate, Exposure, and Effects Model. *International Journal of Life Cycle Assessment* **2009**, *14* (3), 282–284. https://doi.org/10.1007/s11367-009-0066-8.

(6) Rosenbaum, R. K.; Bachmann, T. M.; Gold, L. S.; Huijbregts, M. A. J.; Jolliet, O.; Juraske, R.; Koehler, A.; Larsen, H. F.; MacLeod, M.; Margni, M.; McKone, T. E.; Payet, J.; Schuhmacher, M.; Van De Meent, D.; Hauschild, M. Z. USEtox—the UNEP-SETAC Toxicity Model: Recommended Characterisation Factors for Human Toxicity and Freshwater Ecotoxicity in Life Cycle Impact Assessment. *Int J Life Cycle Assess* **2008**, *13* (7), 532–546. https://doi.org/10.1007/s11367-008-0038-4.

(7) Huijbregts, M. A. J.; Struijs, J.; Goedkoop, M.; Heijungs, R.; Jan Hendriks, A.; Van De Meent, D. Human Population Intake Fractions and Environmental Fate Factors of Toxic Pollutants in Life Cycle Impact Assessment. *Chemosphere* **2005**, *61* (10), 1495–1504. https://doi.org/10.1016/j.chemosphere.2005.04.046.

(8) Van Zelm, R.; Stam, G.; Huijbregts, M. A. J.; Van De Meent, D. Making Fate and Exposure Models for Freshwater Ecotoxicity in Life Cycle Assessment Suitable for Organic Acids and Bases. *Chemosphere* **2013**, *90* (2), 312–317. https://doi.org/10.1016/j.chemosphere.2012.07.014.

(9) Hartmann, J.; Moosdorf, N.; Lauerwald, R.; Hinderer, M.; West, A. J. Global Chemical Weathering and Associated P-Release — The Role of Lithology, Temperature and Soil Properties. *Chemical Geology* **2014**, *363*, 145–163. https://doi.org/10.1016/j.chemgeo.2013.10.025.

(10) Rimstidt, J. D.; Brantley, S. L.; Olsen, A. A. Systematic Review of Forsterite Dissolution Rate Data. *Geochimica et Cosmochimica Acta* **2012**, *99*, 159–178. https://doi.org/10.1016/j.gca.2012.09.019.

(11) Cobo, S. Enhanced Weathering Datasets, 2026. https://doi.org/10.5281/zenodo.16094445.

(12) Hangx, S. J. T.; Spiers, C. J. Coastal Spreading of Olivine to Control Atmospheric CO2 Concentrations: A Critical Analysis of Viability. *International Journal of Greenhouse Gas Control* **2009**, *3* (6), 757–767. https://doi.org/10.1016/j.ijggc.2009.07.001.

(13) Renforth, P. The Negative Emission Potential of Alkaline Materials. *Nature Communications* **2019**, *10* (1), 1401. https://doi.org/10.1038/s41467-019-09475-5.

(14) Foteinis, S.; Campbell, J. S.; Renforth, P. Life Cycle Assessment of Coastal Enhanced Weathering for Carbon Dioxide Removal from Air. *Environmental Science and Technology* **2023**, *57* (15), 6169–6178. https://doi.org/10.1021/acs.est.2c08633.

(15) Strefler, J.; Amann, T.; Bauer, N.; Kriegler, E.; Hartmann, J. Potential and Costs of Carbon Dioxide Removal by Enhanced Weathering of Rocks. *Environmental Research Letters* **2018**, *13* (3), 034010. https://doi.org/10.1088/1748-9326/aaa9c4.

(16) Rinder, T.; Von Hagke, C. The Influence of Particle Size on the Potential of Enhanced Basalt Weathering for Carbon Dioxide Removal - Insights from a Regional Assessment. *Journal of Cleaner Production* **2021**, *315*, 128178. https://doi.org/10.1016/j.jclepro.2021.128178.

(17) Jerden, J.; Mejbel, M.; Filho, A. N. Z.; Carroll, M.; Campe, J. The Impact of Geochemical and Life-Cycle Variables on Carbon Dioxide Removal by Enhanced Rock Weathering: Development and Application of the Stella ERW Model. *Applied Geochemistry* **2024**, *167*, 106002. https://doi.org/10.1016/j.apgeochem.2024.106002.

(18) Montserrat, F.; Renforth, P.; Hartmann, J.; Leermakers, M.; Knops, P.; Meysman, F. J. R. Olivine Dissolution in Seawater: Implications for CO2 Sequestration through Enhanced Weathering in Coastal Environments. *Environmental Science and Technology* **2017**, *51* (7), 3960–3972. https://doi.org/10.1021/acs.est.6b05942.

(19) Flipkens, G.; Fuhr, M.; Fiers, G.; Meysman, F. J. R.; Town, R. M.; Blust, R. Enhanced Olivine Dissolution in Seawater through Continuous Grain Collisions. *Geochimica et Cosmochimica Acta* **2023**, *359*, 84–99. https://doi.org/10.1016/j.gca.2023.09.002.
(20) Amann, T.; Hartmann, J.; Struyf, E.; De Oliveira Garcia, W.; Fischer, E. K.; Janssens, I.; Meire, P.; Schoelynck, J. Enhanced Weathering and Related Element Fluxes - A Cropland Mesocosm Approach. *Biogeosciences* **2020**, *17* (1), 103–119. https://doi.org/10.5194/bg-17-103-2020.
(21) Renforth, P.; Pogge von Strandmann, P. A. E.; Henderson, G. M. The Dissolution of Olivine Added to Soil: Implications for Enhanced Weathering. *Applied Geochemistry* **2015**, *61*, 109–118. https://doi.org/10.1016/J.APGEOCHEM.2015.05.016.
(22) Vienne, A.; Poblador, S.; Portillo-Estrada, M.; Hartmann, J.; Ijiehon, S.; Wade, P.; Vicca, S. Enhanced Weathering Using Basalt Rock Powder: Carbon Sequestration, Co-Benefits and Risks in a Mesocosm Study With Solanum Tuberosum. *Front. Clim.* **2022**, *4*, 869456. https://doi.org/10.3389/fclim.2022.869456.
(23) Beerling, D. J.; Epihov, D. Z.; Kantola, I. B.; Masters, M. D.; Reershemius, T.; Planavsky, N. J.; Reinhard, C. T.; Jordan, J. S.; Thorne, S. J.; Weber, J.; Val Martin, M.; Freckleton, R. P.; Hartley, S. E.; James, R. H.; Pearce, C. R.; DeLucia, E. H.; Banwart, S. A. Enhanced Weathering in the US Corn Belt Delivers Carbon Removal with Agronomic Benefits. *Proc. Natl. Acad. Sci. U.S.A.* **2024**, *121* (9), e2319436121. https://doi.org/10.1073/pnas.2319436121.
(24) Lewis, A. L.; Sarkar, B.; Wade, P.; Kemp, S. J.; Hodson, M. E.; Taylor, L. L.; Yeong, K. L.; Davies, K.; Nelson, P. N.; Bird, M. I.; Kantola, I. B.; Masters, M. D.; DeLucia, E.; Leake, J. R.; Banwart, S. A.; Beerling, D. J. Effects of Mineralogy, Chemistry and Physical Properties of Basalts on Carbon Capture Potential and Plant-Nutrient Element Release via Enhanced Weathering. *Applied Geochemistry* **2021**, *132*, 105023. https://doi.org/10.1016/j.apgeochem.2021.105023.
(25) Kantola, I. B.; Masters, M. D.; Blanc-Betes, E.; Gomez-Casanovas, N.; DeLucia, E. H. Long-term Yields in Annual and Perennial Bioenergy Crops in the Midwestern United States. *GCB Bioenergy* **2022**, *14* (6), 694–706. https://doi.org/10.1111/gcbb.12940.
(26) Wu, W.; Qu, S.; Nel, W.; Ji, J. The Influence of Natural Weathering on the Behavior of Heavy Metals in Small Basaltic Watersheds: A Comparative Study from Different Regions in China. *Chemosphere* **2021**, *262*, 127897. https://doi.org/10.1016/j.chemosphere.2020.127897.
(27) Madankan, M.; Kantzas, E. P.; Espinosa, R. M. E.; Vetter, S. H.; Koh, L.; Smith, P.; Beerling, D. J.; Renforth, P. Larger Rock Extraction Sites Could Improve the Efficiency of Enhanced Rock Weathering in the United Kingdom. *Commun Earth Environ* **2025**, *6* (1), 666. https://doi.org/10.1038/s43247-025-02656-9.
(28) Pehl, M.; Schreyer, F.; Luderer, G. Modelling Long-Term Industry Energy Demand and CO_2 Emissions in the System Context Using REMIND (Version 3.1.0). *Geoscientific Model Development* **2024**, *17* (5), 2015–2038. https://doi.org/10.5194/gmd-17-2015-2024.
(29) Riahi, K.; van Vuuren, D. P.; Kriegler, E.; Edmonds, J.; O'Neill, B. C.; Fujimori, S.; Bauer, N.; Calvin, K.; Dellink, R.; Fricko, O.; Lutz, W.; Popp, A.; Cuaresma, J. C.; KC, S.; Leimbach, M.; Jiang, L.; Kram, T.; Rao, S.; Emmerling, J.; Ebi, K.; Hasegawa, T.; Havlik, P.; Humpenöder, F.; Da Silva, L. A.; Smith, S.; Stehfest, E.; Bosetti, V.; Eom, J.; Gernaat, D.; Masui, T.; Rogelj, J.; Strefler, J.; Drouet, L.; Krey, V.; Luderer, G.; Harmsen, M.; Takahashi, K.; Baumstark, L.; Doelman, J. C.; Kainuma, M.; Klimont, Z.; Marangoni, G.; Lotze-Campen, H.; Obersteiner, M.; Tabeau, A.; Tavoni, M. The Shared Socioeconomic Pathways and Their Energy, Land Use, and Greenhouse Gas Emissions Implications: An Overview. *Global Environmental Change* **2017**, *42*, 153–168. https://doi.org/10.1016/J.GLOENVCHA.2016.05.009.
(30) Beerling, D. J.; Kantzas, E. P.; Lomas, M. R.; Wade, P.; Eufrasio, R. M.; Renforth, P.; Sarkar, B.; Andrews, M. G.; James, R. H.; Pearce, C. R.; Mercure, J. F.; Pollitt, H.; Holden, P. B.; Edwards, N. R.; Khanna, M.; Koh, L.; Quegan, S.; Pidgeon, N. F.; Janssens, I. A.; Hansen, J.; Banwart, S. A. Potential for Large-Scale CO2 Removal via Enhanced Rock Weathering with Croplands. *Nature* **2020**, *583* (7815), 242–248. https://doi.org/10.1038/s41586-020-2448-9.
(31) Tu, Y.; Rafols, R.; Xu, Y.; Butler, N.; Ababneh, L.; Tao, F.; Ramanathan, V.; Houlton, B. Z.; Liao, C. Scaling up Enhanced Rock Weathering for Equitable Climate Change Mitigation. *Commun. Sustain.* **2026**, *1* (1), 32. https://doi.org/10.1038/s44458-026-00034-w.
(32) Cobo, S.; Negri, V.; Valente, A.; Reiner, D. M.; Hamelin, L.; Dowell, N. M.; Guillén-Gosálbez, G. Sustainable Scale-up of Negative Emissions Technologies and Practices: Where to Focus. *Environ. Res. Lett.* **2023**, *18* (2), 023001. https://doi.org/10.1088/1748-9326/acacb3.
(33) Anda, M. Cation Imbalance and Heavy Metal Content of Seven Indonesian Soils as Affected by Elemental Compositions of Parent Rocks. *Geoderma* **2012**, *189–190*, 388–396. https://doi.org/10.1016/j.geoderma.2012.05.009.
(34) Alloway, B. J. *Heavy Metals in Soils. Trace Metals in Metalloids and Soils and Their Bioavailability.*; Alloway, B. J., Trevor, J. T., Eds.; Springer, 2013; Vol. 22.

(35) Wang, H.; Li, X.; Chen, Y.; Li, Z.; Hedding, D. W.; Nel, W.; Ji, J.; Chen, J. Geochemical Behavior and Potential Health Risk of Heavy Metals in Basalt-Derived Agricultural Soil and Crops: A Case Study from Xuyi County, Eastern China. *The Science of the total environment* **2020**, *729*, 139058. https://doi.org/10.1016/j.scitotenv.2020.139058.
(36) Buckingham, F.; Henderson, G. M.; Holdship, P.; Renforth, P. Soil Core Study Indicates Limited CO2 Removal by Enhanced Weathering in Dry Croplands in the UK. *Applied Geochemistry* **2022**, *147*, 105482. https://doi.org/10.1016/j.apgeochem.2022.105482.
(37) Kelland, M. E.; Wade, P. W.; Lewis, A. L.; Taylor, L. L.; Sarkar, B.; Andrews, M. G.; Lomas, M. R.; Cotton, T. E. A.; Kemp, S. J.; James, R. H.; Pearce, C. R.; Hartley, S. E.; Hodson, M. E.; Leake, J. R.; Banwart, S. A.; Beerling, D. J. Increased Yield and CO2 Sequestration Potential with the C4 Cereal Sorghum Bicolor Cultivated in Basaltic Rock Dust-Amended Agricultural Soil. *Global Change Biology* **2020**, *26* (6), 3658–3676. https://doi.org/10.1111/gcb.15089.
(38) Bourg, A. C. M.; Loch, J. P. G. Mobilization of Heavy Metals as Affected by pH and Redox Conditions. In *Biogeodynamics of Pollutants in Soils and Sediments*; 1995; pp 87–102. https://doi.org/10.1007/978-3-642-79418-6_4.
(39) McClain, C. N.; Maher, K. Chromium Fluxes and Speciation in Ultramafic Catchments and Global Rivers. *Chemical Geology* **2016**, *426*, 135–157. https://doi.org/10.1016/j.chemgeo.2016.01.021.
(40) Sharma, N.; Wang, Z.; Catalano, J. G.; Giammar, D. E. Dynamic Responses of Trace Metal Bioaccessibility to Fluctuating Redox Conditions in Wetland Soils and Stream Sediments. *ACS Earth Space Chem.* **2022**, *6* (5), 1331–1344. https://doi.org/10.1021/acsearthspacechem.2c00031.
(41) Hartmann, J.; West, A. J.; Renforth, P.; Köhler, P.; De La Rocha, C. L.; Wolf-Gladrow, D. A.; Dürr, H. H.; Scheffran, J. Enhanced Chemical Weathering as a Geoengineering Strategy to Reduce Atmospheric Carbon Dioxide, Supply Nutrients, and Mitigate Ocean Acidification. *Reviews of Geophysics* **2013**, *51* (2), 113–149. https://doi.org/10.1002/rog.20004.
(42) Holden, F. J.; Davies, K.; Bird, M. I.; Hume, R.; Green, H.; Beerling, D. J.; Nelson, P. N. In-Field Carbon Dioxide Removal via Weathering of Crushed Basalt Applied to Acidic Tropical Agricultural Soil. *Science of the Total Environment* **2024**, *955* (September), 176568. https://doi.org/10.1016/j.scitotenv.2024.176568.
(43) Xu, T.; Yuan, Z.; Vicca, S.; Goll, D. S.; Li, G.; Lin, L.; Chen, H.; Bi, B.; Chen, Q.; Li, C.; Wang, X.; Wang, C.; Hao, Z.; Fang, Y.; Beerling, D. J. Enhanced Silicate Weathering Accelerates Forest Carbon Sequestration by Stimulating the Soil Mineral Carbon Pump. *Global Change Biology* **2024**, *30* (8), 1–17. https://doi.org/10.1111/gcb.17464.
(44) Xu, T.; Li, H.; Vicca, S.; Goll, D. S.; Beerling, D. J.; Chen, Q.; Bi, B.; Yang, Z.; Wang, X.; Yuan, Z. Enhanced Rock Weathering Promotes Soil Organic Carbon Accumulation: A Global Meta-Analysis Based on Experimental Evidence. *Global Change Biology* **2025**, *31* (9), e70483. https://doi.org/10.1111/gcb.70483.
(45) Goll, D. S.; Ciais, P.; Amann, T.; Buermann, W.; Chang, J.; Eker, S.; Hartmann, J.; Janssens, I.; Li, W.; Obersteiner, M.; Penuelas, J.; Tanaka, K.; Vicca, S. Potential CO2 Removal from Enhanced Weathering by Ecosystem Responses to Powdered Rock. *Nature Geoscience* **2021**, *14* (8), 545–549. https://doi.org/10.1038/s41561-021-00798-x.
(46) Vakilifard, N.; Kantzas, E. P.; Edwards, N. R.; Holden, P. B.; Beerling, D. J. The Role of Enhanced Rock Weathering Deployment with Agriculture in Limiting Future Warming and Protecting Coral Reefs. *Environmental Research Letters* **2021**, *16* (9), 094005. https://doi.org/10.1088/1748-9326/ac1818.
(47) Flipkens, G.; Fuhr, M.; Fiers, G.; Meysman, F. J. R.; Town, R. M.; Blust, R. Enhanced Olivine Dissolution in Seawater through Continuous Grain Collisions. *Geochimica et Cosmochimica Acta* **2023**, *359*, 84–99. https://doi.org/10.1016/j.gca.2023.09.002.
(48) Fischer, H. *A History of the Central Limit Theorem: From Classical to Modern Probability Theory*; Springer: New York, NY, 2011. https://doi.org/10.1007/978-0-387-87857-7.